

THE STUDY OF A SYSTEM OF H II REGIONS TOWARD  $l = 24^\circ.8$ ,  $b = 0^\circ.1$  AT THE GALACTIC BAR - NORMA ARM INTERFACEL. K. DEWANGAN<sup>1</sup>, J. S. DHANYA<sup>2</sup>, D. K. OJHA<sup>3</sup>, AND I. ZINCHENKO<sup>4</sup>

## ABSTRACT

To probe the star formation (SF) process, we present a thorough multi-wavelength investigation of several H II regions located toward  $l = 24^\circ.8$ ,  $b = 0^\circ.1$ . A system of at least five H II regions including the mid-infrared bubble N36 (hereafter “system N36”; extension  $\sim 35$  pc) is observationally investigated, and is located at a distance of 6.0 kpc. With this distance, the system N36 is found to be situated at the interface of the Galactic bar and the Norma Galactic arm in our Galaxy, where one may expect the collisions of molecular clouds due to the bar potential. Each H II region (dynamical age  $\sim 0.4$ – $1.3$  Myr) in the system is powered by an O-type star. The system contains 27 ATLASGAL dust clumps at  $870 \mu\text{m}$ . Several clumps are massive ( $> 10^3 M_\odot$ ), and have high bolometric luminosity ( $> 10^3 L_\odot$ ). Using the GRS  $^{13}\text{CO}$  line data, in the direction of the system N36, two velocity components are found around 109 and 113  $\text{km s}^{-1}$ , and are linked in the velocity space. The morphological analysis of  $^{13}\text{CO}$  favours the presence of interacting molecular clouds in the system. Four H II regions and two 6.7 GHz masers are spatially observed at the common areas of the two clouds. The analysis of the *Spitzer* photometric data also traces the noticeable SF activity in the system. Considering the observational outcomes, the formation of O-type stars (including ongoing SF) in the system appears to be triggered by the collisions of molecular clouds at the bar-arm interface.

*Subject headings:* dust, extinction – H II regions – ISM: clouds – ISM: individual objects (N36) – stars: formation – stars: pre-main sequence

## 1. INTRODUCTION

The physical processes involved in the formation of massive O-type stars and their feedback mechanisms are still under debate (Zinnecker & Yorke 2007; Tan et al. 2014). The energetics of O-type stars can affect the origin of new low-mass and massive stars (Deharveng et al. 2010). The massive stars are often surrounded by the bubbles/rings/semi-ring-like structures traced at mid-infrared (MIR)  $8.0 \mu\text{m}$  (Churchwell et al. 2006, 2007), and are also associated with the extended radio continuum emission (e.g., Deharveng et al. 2010). Note that the majority of the studies related to the MIR bubbles are mainly carried out for a single H II region or several H II regions on scales of a few parsecs (e.g., Zinnecker & Yorke 2007; Deharveng et al. 2010; Rathborne et al. 2011; Tackenberg et al. 2012; Simpson et al. 2012; Kendrew et al. 2012; Thompson et al. 2012; Tan et al. 2014; Dewangan et al. 2015a,b; Xu et al. 2016a). However, to our knowledge, in the Milky Way, there is still a limited detailed multi-wavelength study of large-scale systems ( $> 25$  pc) of several MIR bubbles/H II regions containing O-type stars, and hence the origin of such extended system of H II regions still remains unexplored. These systems could be candidates of “mini-starburst” (such as W43 ‘mini-starburst’ region; Motte et al. 2003). With the availability of the radio recombination line (RRL) and

continuum observations (e.g., Lockman 1989; Condon et al. 1998; Anderson & Bania 2009; Jones & Dickey 2012), the MIR survey (e.g., Benjamin et al. 2003), the dust continuum survey at  $870 \mu\text{m}$  (e.g., Schuller et al. 2009; Urquhart et al. 2018), and the  $^{13}\text{CO}$  line survey (e.g., Jackson et al. 2006; Anderson et al. 2009), it appears that the H II regions located toward the Galactic plane and the inner Galaxy are the promising sites to investigate the extended systems of O-type stars. Such study will enable us to understand the physical conditions in a densely clustered environment linked with the luminous giant H II regions/massive star-forming complexes/mini-starburst candidates in the Galaxy. However, in particular, in the direction of the inner Galaxy, the investigation of an extended system of H II regions is often restricted by the near-far kinematic distance ambiguity (e.g., Anderson & Bania 2009; Jones & Dickey 2012; Urquhart et al. 2018). In recent years, a significant effort has been devoted to resolve the distance ambiguity for H II regions in the inner Galaxy (see Urquhart et al. 2018, and references therein). In this work, we aim to observationally investigate a large-scale system/configuration of several H II regions powered by O-type stars and the origin of such a large system.

Several extended H II regions are known in the direction of  $l = 23^\circ.9$  –  $24^\circ.9$  (e.g., Lockman 1989; Kuchar & Clark 1997; Kantharia et al. 2007; Jones & Dickey 2012) (see Figure 1a using the VLA Galactic Plane Survey (VGPS;  $\lambda = 21$  cm; Stil et al. 2006)). Several MIR bubbles (such as, N32, N33, N34, N35, and N36; Churchwell et al. 2006; Deharveng et al. 2010; Simpson et al. 2012) are also reported in the selected longitude range, and are associated with the H II regions (e.g., Anderson & Bania 2009; Urquhart et al. 2013b). In this longitude range, we have examined the spatial distribution

lokeshd@prl.res.in

<sup>1</sup> Physical Research Laboratory, Navrangpura, Ahmedabad - 380 009, India.<sup>2</sup> Malaviya National Institute of Technology (MNIT), Jaipur 302 017, India.<sup>3</sup> Department of Astronomy and Astrophysics, Tata Institute of Fundamental Research, Homi Bhabha Road, Mumbai 400 005, India.<sup>4</sup> Institute of Applied Physics of the Russian Academy of Sciences, 46 Ulyanov st., Nizhny Novgorod 603950, Russia.

of the 21 cm continuum emission and the dust continuum clumps at 870  $\mu\text{m}$  (from Urquhart et al. 2018) (see Figure 1a). Urquhart et al. (2018) solved the distance ambiguity for the clumps using a combination of the HI analysis, maser parallax, and spectroscopic measurements (see their paper for more details). Based on this exercise, three different “clusters” of dense gas clumps are identified in the direction of  $l = 23^\circ.9 - 24^\circ.9$ , which are located at distances of 5.8 kpc (radial velocity ( $V_{lsr}$ ) range = [80, 100]  $\text{km s}^{-1}$ ), 6.0 kpc ( $V_{lsr}$  range = [104, 113]  $\text{km s}^{-1}$ ), and  $\sim 7.8$  kpc ( $V_{lsr}$  range = [115, 122]  $\text{km s}^{-1}$ ). One of the clusters is located toward the ionized regions hosting the MIR bubble N35 at a distance of  $\sim 7.8$  kpc, while the second one is found toward the H II regions associated with the MIR bubble N36 at a distance of 6 kpc. The third one is seen in the direction of the bubbles N33 and N34 at a distance of 5.8 kpc. This analysis also indicates the existence of at least three different physical systems/velocity components in the projected sky area toward  $l = 23^\circ.9 - 24^\circ.9$ . More recently, Torii et al. (2017b) studied the giant molecular cloud (GMC) associated with the MIR bubble N35, which is not physically associated with the bubbles N33, N34, and N36. Similarly, the bubble N36 does not have any physical connection with the bubbles N33 and N34.

In this paper, using multi-frequency data sets (see Table 1), we carry out a detailed investigation of the system of the H II regions associated with the MIR bubble N36 in the direction of  $l = 24^\circ.6 - 24^\circ.9$  (see an area enclosed by a box in Figure 1a). Hereafter, we refer this configuration to “system N36”, which is an extended and a single configuration of several dust clumps (having  $d = 6.0$  kpc and  $V_{lsr}$  range = [104, 113]  $\text{km s}^{-1}$ ) and H II regions/21 cm bright continuum sources. Previously, the MIR bubble N36 ( $l = 024^\circ.837$ ;  $b = +00^\circ.090$ ; Churchwell et al. 2006) was characterized as a broken or incomplete ring with a mean radius and thickness of 2'82 (or 4.9 pc at  $d = 6.0$  kpc) and 0'87 (or 1.5 pc at  $d = 6.0$  kpc), respectively. In the direction of the bubble N36, Kantharia et al. (2007) reported an extended H II region G24.83+0.10 containing multiple radio peaks, and the H II region G24.83+0.10 was suggested to be powered by a single star of spectral type O5.5 (Kantharia et al. 2007). The bubble N36 was also suggested to be a good candidate for triggered massive star formation (e.g., Deharveng et al. 2010).

Using the Galactic structure models and different observational tracers (such as H II regions, GMCs, 6.7 GHz methanol masers etc.), several efforts have been made to understand the Galactic structure/spiral structure of our Galaxy (e.g. Reid et al. 2014; Sato et al. 2014; Hou et al. 2009; Hou & Han 2014; Hu et al. 2016, and references therein). Such studies help us to infer the physical association of the observed tracers with the spiral arms (e.g., Perseus, Carina-Sagittarius, Norma (and Outer arm), Crux-Scutum, Local) of the Milky Way (e.g. Hou et al. 2009; Hou & Han 2014; Xu et al. 2016b, and references therein). The locations of these spiral arms are presented in Figure 1 in Elia et al. (2017). Sato et al. (2014) listed the names of massive star-forming sites located in the Scutum Arm (see Table 2 in their paper). With the help of the literature, it appears that the system N36 ( $l = 24^\circ.6 - 24^\circ.9$  and  $d = 6.0$  kpc) is not part of the Scutum Arm (see Figure 5 in Hou & Han 2014), and is located

in the inner Galaxy, where the Galactic bar meets the Norma Galactic arm in the Milky Way (see also Figure 9 in Nguyen Luong et al. 2011). It has also been suggested that the Norma Spiral arm harbors the most massive GMCs and the most luminous regions of massive star formation in the Milky Way (e.g., Bronfman 2008). Using the *Spitzer* 3.6–8.0  $\mu\text{m}$  data, Benjamin et al. (2005) reported the presence of a Galactic bar having a radius of 4.4 kpc in the Milky Way, which is oriented about  $44^\circ$  relative to the Sun-Galactic center line. Together, the system N36 is an interesting target field, where one can carry out an investigation of the bar-arm interaction (e.g., Nguyen Luong et al. 2011; Beuther et al. 2017).

In this paper, we have focused our analysis in the system N36 to observationally understand the origin of the large-scale configuration of O-type stars. We also study the bar-arm interaction in our selected field. The study of dust clumps against the distribution of young stellar objects (YSOs) is also yet to be analyzed in the system N36. Furthermore, we also examine the physical environment and the impact of massive stars in their vicinity. However, in the direction of  $l = 24^\circ.6 - 24^\circ.9$ ,  $b = -0^\circ.2 - 0^\circ.2$ , a detailed distribution of molecular gas for the system N36 has not been investigated.

The paper is organized in the following way. In Section 2, we provide the information about the adopted data sets. Section 3 presents the results related to the physical environment and point-like sources. In Section 4, we discuss the possible star formation process operating in our selected target region. Finally, the main results are summarized in Section 5.

## 2. DATA SETS AND ANALYSIS

The multi-wavelength data sets adopted in this paper were retrieved from different surveys, which are listed in Table 1 (see Dewangan et al. 2017a,b, 2018a, for more details).

## 3. RESULTS

### 3.1. Physical environment of the system N36

#### 3.1.1. Multi-wavelength view

Figure 1a displays an extended area containing three different “clusters” of dense gas clumps in the direction of  $l = 23^\circ.9 - 24^\circ.9$  (see Section 1). Based on the available observed parameters of the dust clumps (such as positions, distances, and radial velocities) in conjunction with the radio continuum data, we have investigated an extended system of H II regions in the direction of the inner Galaxy (i.e. “system N36”; extension  $\sim 35$  pc; see a box in Figure 1a). In Figures 1b and 1c, the position-velocity plots of the GRS  $^{13}\text{CO}$  ( $J=1-0$ ) ( $\text{rms} \approx 0.13$  K; velocity resolution of  $0.21$   $\text{km s}^{-1}$ ; Jackson et al. 2006) trace different velocity components in the direction of a wide-field area around the system N36 (see Figure 1a). One can see the existence of complex velocity structures between 80 and 125  $\text{km s}^{-1}$  in the velocity space. These plots are displayed in a velocity range from 0 to 125  $\text{km s}^{-1}$ . Note that the molecular gas in the direction of the system N36 is examined in a velocity range of [102, 116]  $\text{km s}^{-1}$ .

In Figures 2a and 2b, we present a zoomed-in view of the system N36 using the SHS H $\alpha$ , GRS  $^{13}\text{CO}$ , and NVSS 1.4 GHz images (size  $\sim 0^\circ.33$  (34.6 pc)  $\times$   $0^\circ.42$  (44.0 pc)).

**Table 1**  
Multi-wavelength surveys adopted in this paper.

Survey	Wavelength(s)	Resolution ( $''$ )	Reference
NRAO VLA Sky Survey (NVSS)	21 cm	$\sim 46$	Condon et al. (1998)
VLA Galactic Plane Survey (VGPS)	21 cm	$\sim 60$	Stil et al. (2006)
Galactic Ring Survey (GRS)	2.7 mm; $^{13}\text{CO}$ ( $J = 1-0$ )	$\sim 45$	Jackson et al. (2006)
APEX Telescope Large Area Survey of the Galaxy (ATLASGAL)	870 $\mu\text{m}$	$\sim 19.2$	Schuller et al. (2009)
<i>Herschel</i> Infrared Galactic Plane Survey (Hi-GAL)	70, 160, 250, 350, 500 $\mu\text{m}$	$\sim 5.8, \sim 12, \sim 18, \sim 25, \sim 37$	Molinari et al. (2010)
<i>Spitzer</i> MIPS Inner Galactic Plane Survey (MIPSGAL)	24 $\mu\text{m}$	$\sim 6$	Carey et al. (2005)
<i>Spitzer</i> Galactic Legacy Infrared Mid-Plane Survey Extraordinaire (GLIMPSE)	3.6, 4.5, 5.8, 8.0 $\mu\text{m}$	$\sim 2, \sim 2, \sim 2$	Benjamin et al. (2003)
SuperCOSMOS H $\alpha$ survey (SHS)	0.6563 $\mu\text{m}$	$\sim 1$	Parker et al. (2005)

Figure 2a displays the SHS H $\alpha$  image overlaid with the NVSS 1.4 GHz continuum emission contours. The NVSS map reveals extended ionized emissions in the system N36, which appear parallel to a line having a Galactic position angle (GPA) of  $215^\circ$  (see solid red lines in Figure 2a). There is no extended diffuse emission seen in the H $\alpha$  image. However, in the Galactic southern side, some noticeable H $\alpha$  emission is observed. It appears that dust extinction is affecting the optical emission from N36. Figure 2b shows the  $^{13}\text{CO}$  emission contours against the NVSS 1.4 GHz radio emission. The integrated intensity map of  $^{13}\text{CO}$  from 102 to 116 km s $^{-1}$  traces a spatial distribution of the molecular gas toward the system N36. In the literature, the clouds C24.81+0.10 ( $V_{lsr} = 108.3$  km s $^{-1}$ ;  $\Delta V = 8.2$  km s $^{-1}$ ) and U24.68–0.16b ( $V_{lsr} = 112.5$  km s $^{-1}$ ;  $\Delta V = 5.1$  km s $^{-1}$ ) are reported toward our selected field. These clouds are also labeled in Figure 2b. In the system N36, the cloud C24.81+0.10 is observed in the Galactic northern direction, whereas the cloud U24.68–0.16b is found in the Galactic southern side. A detailed study of the molecular gas is presented in Section 3.2.

Figures 3a and 3b show a spatial view of the system N36 using the *Herschel* 70  $\mu\text{m}$  and *Spitzer* 8.0  $\mu\text{m}$  images, respectively. The images at 8.0 and 70  $\mu\text{m}$  are overlaid with the NVSS radio continuum emission. The 70  $\mu\text{m}$  image is also overlaid with the ATLASGAL dust continuum clumps at 870  $\mu\text{m}$ . Table 2 lists the physical parameters of the ATLASGAL clumps (i.e. peak flux density, integrated flux density, radial velocity, distance, effective radius, dust temperature, bolometric luminosity, clump mass, and molecular hydrogen column density), which are obtained from Urquhart et al. (2018) (see their paper for more details). Using the molecular line observations (e.g., CO, NH $_3$ , CS etc), Urquhart et al. (2018) reported the measured radial velocity ranges of the ATLASGAL clumps to be 104–113 km s $^{-1}$  (see Table 2). One can find that these 27 clumps (i.e. c1–c27; see squares in Figure 3a) are located at a distance of 6.0 kpc (see Table 2). Three positions of the RRL observations (from Lockman 1989) are also marked in Figure 3a (see star symbols in Figure 3a). These ionized regions are well depicted in the ionized gas velocity range of 108–112 km s $^{-1}$  (e.g., Lockman 1989; Anderson & Bania 2009). Several H II regions (such as G24.85+0.09, G24.80+0.10, G24.74+0.08, G24.71–0.13, and G24.68–0.16) are also highlighted in Figure 3b (e.g., Kantharia et al. 2007). The two compact/ultra-compact H II regions G24.85+0.09 and G24.80+0.10 are seen with an extended H II region G24.83+0.10. All these H II regions are members of the system N36, and are physically associated with each other. We have also marked the observed positions of the Class II 6.7 GHz methanol

masers (from Szymczak et al. 2012) in Figures 3a and 3b, which are well depicted in a velocity range of 110–115 km s $^{-1}$ . These masers are also physically associated with the radio continuum sources (such as G24.85+0.09, G24.80+0.10, and G24.68–0.16), further indicating the presence of massive stars. It is supported by the fact that the 6.7 GHz methanol masers are a reliable tracer of massive YSOs (e.g., Walsh et al. 1998; Urquhart et al. 2013a).

In Figures 4a and 4b, we have superimposed the ATLASGAL 870  $\mu\text{m}$  continuum contours and the  $^{13}\text{CO}$  emission contours on the *Spitzer* 8.0  $\mu\text{m}$  image, respectively. The integrated  $^{13}\text{CO}$  emission contours are shown here only for the comparison purpose. Two previously known clouds (i.e., C24.81+0.10 and U24.68–0.16b) are also labeled in Figure 4b. One of the clouds (i.e. C24.81+0.10) is associated with the H II regions G24.83+0.10 (containing G24.85+0.09 and G24.80+0.10) and G24.74+0.08, while the other one (i.e. U24.68–0.16b) contains the H II regions G24.71–0.13, and G24.68–0.16. In Figure 4b, the positions of the ATLASGAL clumps are also marked, allowing to infer the dense regions in the molecular clouds. An extended dust continuum emission at 870  $\mu\text{m}$  is detected in the direction of each cloud (see Figures 4a and 4b). One can also note that the H II region G24.71–0.13 is seen between the clouds C24.81+0.10 and U24.68–0.16b (see also Figure 2b), where no dense materials at 870  $\mu\text{m}$  and molecular emission are found (see a dashed big circle in Figures 4a and 4b). The dust continuum emission, 6.7 GHz methanol masers, and molecular emission are prominently observed at the edges of the bubble N36. In the direction of the bubble N36, a cavity-like feature is also highlighted in Figures 4a and 4b, where the dust continuum emission and the molecular gas are not observed. Basically, the cavity-like feature represents an interior of the MIR bubble N36 (having an average radius of 4.9 pc). The image at 70  $\mu\text{m}$  depicts the warm dust emission, whereas the 8.0  $\mu\text{m}$  band contains the 7.7 and 8.6  $\mu\text{m}$  polycyclic aromatic hydrocarbon (PAH) emission (including the continuum). Bright and extended emission seen in the 8.0 and 70  $\mu\text{m}$  continuum images is in good agreement, and is found at the locations of the ionized regions. Hence, concerning the system N36, the morphological agreement is seen in all the multi-wavelength images. The spatial distribution of the molecular gas, dust emission, and ionized gas indicates the impact of the H II regions in the system N36.

### 3.1.2. Temperature map and powering sources

The *Herschel* temperature map of the system N36 is shown in Figure 5a. Following the methods given in Mallick et al. (2015), the map is produced using the *Herschel* 160–500  $\mu\text{m}$  data. The temperature map is over-

laid with the NVSS radio continuum emission, indicating that the majority of the H II regions are associated with the warmer emission ( $T_d \sim 23\text{--}32$  K). There is also an extended temperature structure seen in the system N36. The integrated  $^{13}\text{CO}$  emission at  $[102, 116]$  km s $^{-1}$  is also superimposed on the temperature map.

Based on the NVSS radio map ( $1\sigma \sim 0.45$  mJy/beam), in the system N36, we have selected four H II regions (labeled as 1-4) and their positions are marked in Figure 5b. The IDs 1, 2, 3, and 4 refer to the H II regions G24.83+0.10 (containing G24.85+0.09 and G24.80+0.10), G24.74+0.08, G24.71-0.13, and G24.68-0.16, respectively. The boundary of each H II region is highlighted in the 1.4 GHz map (see Figure 5b), which is an outcome of the “*clumpfind*” IDL program (Williams et al. 1994). The 6.7 GHz methanol masers are seen in the H II regions 1 (i.e. G24.85+0.09 and G24.80+0.10) and 4 (i.e. G24.68-0.16). Following the analysis given in Dewangan et al. (2017a, and see references therein), the values of Lyman continuum photon ( $N_{\text{uv}}$ ) and dynamical age ( $t_{\text{dyn}}$ ) are estimated for each H II region using the NVSS radio continuum data, and are listed in Table 3. This exercise reveals the spectral types of the ionizing stars of the H II regions to be O type stars, which are in almost agreement with the results of Kantharia et al. (2007). The  $t_{\text{dyn}}$  values of these H II regions vary between 0.4 and 1.3 Myr (for an initial gas density  $n_0 = 10^3$  cm $^{-3}$ ).

Using the NVSS 1.4 GHz map, we have also estimated the physical properties of the ionized gas (i.e., electron density ( $n_e$ ), emission measure (EM), and mass of ionized hydrogen ( $M_{\text{HII}}$ )). These parameters are also listed in Table 3, and are derived based on the equations given in Panagia & Walmsley (1978) for a roughly spherical geometry case. All the H II regions have high EM values ( $> 10^4$  cm $^{-6}$  pc). The H II regions 1 and 3 have higher values of  $M_{\text{HII}}$  compared to other two H II regions (i.e., IDs 2 and 4; see Table 3).

### 3.1.3. Distribution of clump parameters

We have identified 27 ATLASGAL dust continuum clumps at  $870 \mu\text{m}$  (from Urquhart et al. 2018) toward the system N36 (see Figure 6a and also Table 2). We find that the dust clumps c1-c10 and c18 are embedded in the cloud U24.68–0.16b, while the other ATLASGAL clumps (c11-c17 and c19-c27) are seen toward the cloud C24.81+0.10 (see Figure 4b). It implies that the clouds contain several massive clumps (see Table 2). One can also notice that the majority of the clumps are distributed toward the four ionized regions (see Figure 6a). However, some clumps are also seen away from the NVSS radio continuum emission (see Figure 6a). Figure 6b shows the distribution of the radial velocity of clumps against the Galactic longitude. The radial velocity of clumps toward the ionized regions 1, 2, and 3 are found between 104 and 111 km s $^{-1}$ , while the clumps seen toward the ionized region 4 are depicted with the radial velocity of 109–114 km s $^{-1}$ . These results indicate the presence of two velocity components in the system N36. Figure 6c presents the distribution of the dust temperature of clumps against the Galactic longitude. The figure shows a dust temperature range of  $\sim 23\text{--}35$  K toward the clumps, which are located toward the H II regions. This result is in agreement with the outcome of the *Herschel*

temperature map (see Figure 5a). In Figure 6d, we show the distribution of the bolometric luminosity of clumps against the Galactic longitude, which reveals the presence of high luminosity clumps ( $> 10^3 L_{\odot}$ ) toward the ionized regions in the system N36. In Figure 6e, we display the distribution of clump masses against the Galactic longitude. The clump masses vary between 185 and 7635  $M_{\odot}$ . Massive clumps ( $> 10^3 M_{\odot}$ ) are mainly seen toward all the ionized regions. Figure 6f shows the distribution of the ratio of the bolometric luminosity and mass of clumps (i.e.,  $L_{\text{bol}}/M_{\text{clump}}$ ) against the Galactic longitude. The ratio  $L_{\text{bol}}/M_{\text{clump}}$  of clumps is considered as an indicator of clumps evolution (e.g., Molinari et al. 2016). The clumps with  $L_{\text{bol}}/M_{\text{clump}} > 10$  indicate their association with the H II regions (e.g., Molinari et al. 2016). We find 9 ATLASGAL clumps having  $L_{\text{bol}}/M_{\text{clump}} > 10$  in the system N36 (see Figure 6f). The hydrogen column density range varies between  $8.0 \times 10^{21}$  and  $1.0 \times 10^{23}$  cm $^{-2}$ . Furthermore, the 6.7 GHz methanol masers are associated with the dust clumps c7, c19, and c26, which have high bolometric luminosities (i.e.,  $4\text{--}15 \times 10^4 L_{\odot}$ ) and clump masses (i.e., 400–7635  $M_{\odot}$ ).

### 3.2. Kinematics of molecular gas

In this section, to probe the kinematics of molecular gas in the system N36, the study of molecular gas is carried out using the GRS  $^{13}\text{CO}$  ( $J=1\text{--}0$ ) line data.

In the direction of the system N36, the radial velocity ( $V_{\text{lsr}}$ ) ranges of the ionized gas, the molecular gas, and the 6.7 GHz methanol masers are reported to be 108–112, 105–114, and 110–116 km s $^{-1}$ , respectively. Figure 7 shows the integrated  $^{13}\text{CO}$  velocity channel maps (starting from 101 km s $^{-1}$  at intervals of 1 km s $^{-1}$ ), where the locations of the ionized emission are also marked. The velocity channel maps trace at least two molecular components (around 109 and 113 km s $^{-1}$ ) along the line of sight in the system N36 (see arrows in Figure 7). In the system N36, there is an extended GMC seen in the velocity between 103 and 110 km s $^{-1}$ , and there exists also another cloud component in the velocity between 111 and 115 km s $^{-1}$ . In the support of these results, in Figure 8a, we have presented integrated velocity maps at  $[108, 109]$  km s $^{-1}$  and  $[112, 113]$  km s $^{-1}$  overlaid with the radio continuum emission. There are some areas in the system N36, where the molecular emissions observed in both the integrated velocity maps are distributed. In Figure 8b, we show the  $^{13}\text{CO}$  first-order moment map, revealing the mean  $V_{\text{lsr}}$  of  $^{13}\text{CO}$  at each grid point. The map is also superimposed with the integrated molecular emission contour at  $[102, 116]$  km s $^{-1}$ , as shown in Figures 2b and 4b. The velocity gradients are observed in the clouds C24.81+0.10 and U24.68–0.16b.

To study the velocity field in the direction of the system N36, the integrated intensity map and position-velocity maps of  $^{13}\text{CO}$  are presented in Figure 9. For the comparison purpose, the integrated  $^{13}\text{CO}$  emission at  $[102, 116]$  km s $^{-1}$  is shown in Figure 9a. Figures 9b and 9d display the latitude-velocity and longitude-velocity maps of  $^{13}\text{CO}$ , respectively. In both the position-velocity maps, we have also highlighted two velocities (i.e. 109 and 113 km s $^{-1}$ ). These two velocity components appear to be linked through a relatively weak  $^{13}\text{CO}$  emission. In the

position-velocity maps, these two clouds are separated by  $4\text{--}12\text{ km s}^{-1}$  in velocity. In Figure 9c, we have shown the spatial distribution of the molecular gas in the two clouds at  $103\text{--}110.5\text{ km s}^{-1}$  and  $111\text{--}115\text{ km s}^{-1}$ . Interestingly, the two clouds exhibit mutually overlapping areas (see also Figure 8a).

Figures 10a and 10b also show the spatial distribution of the molecular gas in the clouds at  $103\text{--}110.5$  and  $111\text{--}115\text{ km s}^{-1}$  against the NVSS 1.4 GHz continuum emission, respectively. One can notice that the majority of the molecular gas in the cloud C24.81+0.10 (at  $103\text{--}110.5\text{ km s}^{-1}$ ) is seen toward the MIR bubble N36, and a noticeable molecular emission is also distributed toward the H II region G24.68-0.16 (or cloud U24.68-0.16b). Similarly, a majority of the molecular gas in the cloud U24.68-0.16b (at  $111\text{--}115\text{ km s}^{-1}$ ) is found in the direction of the H II region G24.68-0.16, and a noticeable molecular gas is also traced toward the bubble N36 (or cloud C24.81+0.10). These results indicate that the clouds C24.81+0.10 and U24.68-0.16b are extended GMCs, and their central parts are severely affected by the ionized emission. This is the reason that there are no molecular and dust emissions found in the central parts of the clouds. In Figure 10c, we have also displayed the spatial distribution of the  $^{13}\text{CO}$  emission integrated over two different velocity ranges (i.e.  $103\text{--}110.5$  and  $111\text{--}115\text{ km s}^{-1}$ ) against the NVSS 1.4 GHz radio continuum emission. Four H II regions (i.e. G24.80+0.10, G24.74+0.08, G24.71-0.13, and G24.68-0.16) are found in the common areas of the clouds. As mentioned earlier, the H II regions G24.80+0.10 and G24.68-0.16 contain the 6.7 GHz masers. Hence, the ongoing massive star formation activity is evident toward the common zones of the clouds. Figure 10d shows the spatial distribution of the ATLASGAL  $870\text{ }\mu\text{m}$  continuum emission against the NVSS 1.4 GHz radio continuum emission. A cavity-like feature is highlighted in the bubble N36, where the molecular and dust continuum emissions are absent (see Figures 10a and 10d). A solid line having the GPA of  $215^\circ$  is also highlighted in Figures 10a, 10b, and 10d. The cavity-like feature seen in the cloud at  $103\text{--}110.5\text{ km s}^{-1}$  appears remarkably parallel to the molecular cloud at  $111\text{--}115\text{ km s}^{-1}$  located in the southern direction (see arrows in Figure 10c). These features are organized along the line with the GPA of  $215^\circ$ . Discussion on these results are presented in Section 4.

### 3.3. Embedded protostars and their distribution

This section deals with the selection of the embedded protostars in our selected target field. To detect infrared excess emission from the protostars, we have employed the *Spitzer* photometric data. To select protostars, Hartmann et al. (2005) and Getman et al. (2007) explored the color-color ( $[4.5]\text{--}[5.8]$  vs  $[3.6]\text{--}[4.5]$ ) space using the *Spitzer* 3.6, 4.5, and 5.8 photometric data, and provided the selection conditions (i.e.  $[4.5]\text{--}[5.8] \geq 0.7\text{ mag}$  and  $[3.6]\text{--}[4.5] \geq 0.7\text{ mag}$ ). Figure 11a shows a color-color plot ( $[4.5]\text{--}[5.8]$  vs  $[3.6]\text{--}[4.5]$ ) of point-like sources. Based on the color conditions, we have identified 125 protostars, which are shown by red circles in Figure 11a. There is also possibility that our selected protostars might be contaminated by asymptotic giant branch (AGB) stars. Using the *Spitzer* 4.5- $24\text{ }\mu\text{m}$  bands,

Robitaille et al. (2008) proposed a condition (i.e.  $[4.5] > 7.8\text{ mag}$  and  $[8.0]\text{--}[24.0] < 2.5\text{ mag}$ ) to infer possible AGB contaminants. Based on the availability of the MIPS GAL photometric data at  $24\text{ }\mu\text{m}$  (e.g., Gutermuth & Heyer 2015) for our selected protostars, we followed the work of Robitaille et al. (2008) and tried to identify the possible AGB contaminants. We find that our selected protostars appear to be free from the AGB contaminants.

Figures 11b and 11c display the overlay of the selected protostars (see circles) on the ATLASGAL  $870\text{ }\mu\text{m}$  continuum contour map and the molecular intensity maps, respectively. Figure 11b reveals the spatial correlation between protostars and cold dust emission, tracing the ongoing star formation activity toward the dense regions in the system N36. The protostars, dust emission, and molecular emission are not detected between the northern and southern H II regions (see a dashed big circle in Figures 11b and 11c). In Figure 11c, the filled circles and open circles indicate the distribution of protostars inside and outside the molecular clouds, respectively.

## 4. DISCUSSION

### 4.1. Impact of massive stars in the system N36

In the present work, we have selected a configuration of an extended physical system of O-type stars (i.e. system N36) toward  $l = 24^\circ.8$ ,  $b = 0^\circ.1$ . The system is prominently seen in the *Herschel* temperature and NVSS 1.4 GHz continuum maps (see Figures 2a and 5a). The existence of the extended temperature structure in the system gives a clue of the feedback from massive stars (such as, stellar wind, ultraviolet radiation, and pressure-driven H II region) powering the H II regions. The molecular and dust materials are not observed toward the central parts of the extended clouds C24.81+0.10 and U24.68-0.16b, which probably indicates that the H II regions in the system are interacting with their immediate environment. In the system, several massive clumps ( $> 10^3\text{ M}_\odot$ ) are found. Several embedded protostars (average age  $\sim 0.44\text{ Myr}$ ; Evans et al. 2009) distributed toward the clumps are also identified in the system N36, depicting the ongoing star formation activity. Three 6.7 GHz methanol masers are observed in the system, suggesting the presence of early phases of massive star formation ( $< 0.1\text{ Myr}$ ). The dynamical ages of the H II regions in the system vary between 0.4 and 1.3 Myr (see Section 3.1). Hence, it is possible that some of the H II regions in the system N36 are old enough to influence the formation of embedded protostars (e.g., Elmegreen 1998), which cannot be neglected in the system N36 (e.g., Deharveng et al. 2010).

However, it remains unknown how the system of O-type stars is formed, and which process can be responsible for the observed velocity separation between two clouds (i.e.  $4\text{--}12\text{ km s}^{-1}$ ) seen in the direction of the system N36. To assess the role of the feedback of massive star(s) for explaining the observed velocity separation, we have computed the mechanical energy ( $E_w \sim 3 \times 10^{48}\text{ ergs}$ ) that can be liberated out by the massive O6V star in a given timescale (i.e.  $0.5\text{ Myr}$ ). In the analysis, we have first estimated the expected mechanical luminosity of the stellar wind ( $L_w = 0.5\dot{M}_w V_w^2\text{ erg s}^{-1}$ ) for the O6V star where the mass-loss rate ( $\dot{M}_w =$

$2.0 \times 10^{-7} M_{\odot} \text{ yr}^{-1}$ ; de Jager et al. 1988) and the wind velocity ( $V_w = 2500 \text{ km s}^{-1}$ ; Prinja et al. 1990) are considered. In the next step, we have compared the value of  $E_w$  with the kinematic energy ( $\sim 7.3 \times 10^{48}$  ergs) of the cloud C24.81+0.10 ( $M_{\text{cloud}} \sim 45385 M_{\odot}$ ) at a velocity of  $4 \text{ km s}^{-1}$ . We have also computed the kinematic energy (i.e.  $\sim 2.7 \times 10^{48}$  ergs) of the cloud at 111-115  $\text{km s}^{-1}$  ( $M_{\text{cloud}} \sim 16975 M_{\odot}$ ; see Figure 10b) with a velocity of  $4 \text{ km s}^{-1}$ , which is also comparable to the value of  $E_w$ . These results are also valid for a velocity separation of  $12 \text{ km s}^{-1}$ . Hence, we find that the stellar feedback is even more inefficient for a velocity separation larger than  $4 \text{ km s}^{-1}$ . On the basis of these calculations, we find that the stellar feedback cannot explain the velocity separation between two clouds. It also implies that the feedback of massive stars does not explain the synchronous birth of O stars in the system N36. For estimating the molecular masses of the clouds, we have followed the work of Yan et al. (2016) (see also equations 4 and 5 in their paper).

#### 4.2. Location of the system N36 in the Milky Way

The location of the system of H II regions hosting the bubble N36 in the Milky Way is inferred through the knowledge of its kinematic distance (i.e. 6 kpc), which has been derived with the help of the Galactic rotation curve (e.g., McClure-Griffiths & Dickey 2007; Reid et al. 2009, 2014) and the velocity measurements of the H I/CO/6.7 GHz maser/ionized gas (e.g., Anderson & Bania 2009; Hou & Han 2014; Hu et al. 2016; Urquhart et al. 2018). However, one obtains two possible kinematic distances corresponding to one  $V_{lsr}$  in the inner Galaxy, referred to as kinematic distance ambiguity. In earlier studies, the near-kinematic distance (i.e.  $\sim 6$  kpc) to the H II regions in the system of O-type stars was adopted (see Kantharia et al. 2007; Anderson & Bania 2009; Jones & Dickey 2012, for more details). Hu et al. (2016) reported two 6.7 GHz methanol masers toward the bubble N36 at a distance of  $\sim 9$  kpc, while Hou & Han (2014) listed a distance of  $\sim 6$  kpc for one of the 6.7 GHz methanol masers reported by Hu et al. (2016). Furthermore, Hu et al. (2016) also derived a distance of  $\sim 6$  kpc for another 6.7 GHz methanol maser in the system of H II regions. Based on the extensive work of Urquhart et al. (2018), the kinematic distance ambiguity of the sources in our selected target field has also been resolved.

Hou & Han (2014) studied the distribution of the H II regions against a spiral arm model (see Figure 5 in their paper). They showed the locations of H II regions, different spiral arms, and the Galactic bar in their Figure 5. Following their work, the adopted distance to the system N36 (i.e.  $d = 6.0$  kpc) favours its location ( $l = 24^{\circ}.6 - 24^{\circ}.9$ ) in the direction of the interface of the Galactic bar and the Norma Galactic arm in the Milky Way (see lower right panel in Figure 5 in Hou & Han 2014).

#### 4.3. Star formation scenario in the system N36

In Section 1, based on the knowledge of  $V_{lsr}$  of the ATLASGAL clumps, we have identified at least three different velocity components (i.e. [80, 100], [104, 113], and [115, 122]  $\text{km s}^{-1}$ ) in the direction of  $l = 23^{\circ}.9 - 24^{\circ}.9$  (see Figure 1a). In the velocity space of  $^{13}\text{CO}$ , these velocity components are also seen in this selected longitude direction (see Figures 1b and 1c). The exis-

tence of different velocity components further supports that the system of O-type stars is located in the direction of the bar-arm interface (e.g., Beuther et al. 2017). In the bar-arm interface, there is possibility of the collisions of molecular clouds due to the bar potential. It has also been suggested that colliding streams of gas from the bar and the arm may favour increased star formation (e.g., Nguyen Luong et al. 2011; Beuther et al. 2017).

In recent years, the cloud-cloud collision (CCC) process is being investigated to explain the observed star formation activities at the junction of molecular clouds or the shock-compressed interface (e.g., Habe & Ohta 1992; Anathpindika 2010; Inoue & Fukui 2013; Takahira et al. 2014; Haworth et al. 2015a,b; Torii et al. 2017a; Bisbas et al. 2017; Balfour et al. 2017; Takahira et al. 2018, and references therein). In the CCC process, the maximum star-formation is expected close to the point of impact or collision interface (Haworth et al. 2015a). The spatial and velocity connection of two clouds with a large velocity separation provides a promising hint of the CCC process (e.g., Furukawa et al. 2009; Ohama et al. 2010, 2018a,b; Fukui et al. 2014, 2016, 2018a,b; Baug et al. 2016; Dewangan 2017; Dewangan et al. 2017a,b; Dewangan & Ojha 2017; Dewangan et al. 2018b; Fujita et al. 2017; Torii et al. 2017a,b; Sano et al. 2018). The detection of complementary distributions of clouds is considered as an another important evidence of the CCC process (e.g. Fukui et al. 2018a). In this context, a cavity exists in one of the molecular clouds, and is referred to as ‘‘Keyhole’’ feature or an intensity depression in the molecular distribution. Additionally, the other cloud is referred to as ‘‘Key’’ feature or intensity enhancement, which can be displaced with respect to the ‘‘Keyhole’’ feature (see Fukui et al. 2018a, for more details). These authors utilized a method to estimate the displacement by optimizing the overlap of the intensity enhancement and depression.

In Section 3.2, we have found that there are two molecular cloud components (at 103-110.5 and 111-115  $\text{km s}^{-1}$ ) in the system, which are linked in the velocity space (see the velocity channel maps and position-velocity plots). A spatial separation between the northern edge of U24.68–0.16b (at 111-115  $\text{km s}^{-1}$ ) and the southern edge of C24.81+0.10 (at 103-110.5  $\text{km s}^{-1}$ ) can also be seen in Figure 12a. In Section 4.1, our calculations suggest that the cloud C24.81+0.10 (at 103-110.5  $\text{km s}^{-1}$ ) is more massive compared to the cloud U24.68–0.16b (at 111-115  $\text{km s}^{-1}$ ). A careful examination of the molecular gas at 103-110.5  $\text{km s}^{-1}$  in the system N36, we find a cavity or ‘‘Keyhole’’ configuration in the northern direction along a line with the GPA of  $215^{\circ}$  (see Figure 12a). Additionally, a displaced ‘‘Key’’ feature, traced at 111-115  $\text{km s}^{-1}$ , is identified in the southern direction, and appears remarkably parallel to the ‘‘Keyhole’’ configuration (see Figure 12a). In Figure 12b, we have applied a displacement of  $\sim 33.3$  pc to the cloud at 111-115  $\text{km s}^{-1}$  in the northern direction along a line having the GPA of  $215^{\circ}$  (see a solid line in Figure 12b). This exercise gives a complementary fit between the clouds at 103-110.5 and 111-115  $\text{km s}^{-1}$ , which indicates the interaction of these two clouds in the system N36. The distribution of the dust emission, molecular gas, and protostars is not found between

these clouds (or “Key” and “Keyhole” features), where only ionized emission is observed. The ionized emission is also aligned with the “Key” and “Keyhole” features. Altogether, our results support the existence of interacting molecular clouds in the system N36. We have also traced reliable signatures of massive star formation toward the common zones of the clouds (i.e., C24.81+0.10 and U24.68–0.16b). Hence, the CCC scenario (i.e., the collision between the cloud components around 109 and  $113 \text{ km s}^{-1}$ ) is applicable in the system, which may explain the formation of the H II regions in the system. The lifetime of the collision of molecular clouds is computed to be  $\sim 2.7\text{--}8.2 \text{ Myr}$ . The ages of the H II regions are estimated to be about  $0.4\text{--}1.3 \text{ Myr}$ . These calculations also indicate the onset of the CCC process. In the calculation, we have adopted a viewing angle ( $= 45^\circ$ ) of the collision to the line of sight. Hence, the distance between the two clouds is considered to be  $\sim 47 \text{ pc}$  ( $= 33.3 \text{ pc}/\sin(45^\circ)$ ). The velocity difference estimated from the observed relative velocity is found to be  $\sim 5.6\text{--}17 \text{ km s}^{-1}$  ( $= 4\text{--}12/\cos(45^\circ)$  (in  $\text{km s}^{-1}$ ); see Section 3.2). The lower end in the estimated lifetime of the collision interval (i.e.,  $\sim 2.7 \text{ Myr}$ ) corresponding to the higher end of the velocity range (i.e.,  $12 \times \sqrt{2} \text{ km s}^{-1}$ ) is more consistent with the ages of the H II regions, suggesting a recent onset of massive star formation. Considering the location of the system N36 in the inner Galaxy, optically thin molecular line observations will provide an opportunity to explore further the collision scenario in the system N36.

As mentioned in Section 1, in the direction of  $l = 23^\circ.9 - 24^\circ.9$ , a cluster of the ATLASGAL clumps is found toward the MIR bubble N35, and these clumps are situated at a distance of 7.8 kpc. Torii et al. (2017b) carried out an observational study of the GMC associated with the bubble N35 and two H II regions (i.e., G024.392+00.072, and G024.510-00.060), and adopted a distance of the GMC to 8.8 kpc. They proposed a CCC scenario (i.e., the collisions between the lower-velocity component (LVC) at  $110\text{--}114 \text{ km s}^{-1}$  and three higher-velocity-components (HVCs) at  $118\text{--}126 \text{ km s}^{-1}$ ) to explain the formation of the bubble N35 and two H II regions. They discussed that the collisions between molecular clouds had begun since less than  $\sim 1 \text{ Myr}$  ago. Considering the distances of the bubble N35 and the system N36, our selected target system does not have any physical connection with the bubble N35. However, the CCC scenario in both the systems has been proposed, and the collisions took place in both the systems independently.

## 5. SUMMARY AND CONCLUSIONS

In order to investigate a large-scale system of several MIR bubbles/H II regions hosting the O-type stars and the birth of such extended system, we present the multi-wavelength data analysis of a field (size  $\sim 0^\circ.33 \times 0^\circ.42$ ) containing several H II regions toward  $l = 24^\circ.6 - 24^\circ.9$ ,  $b = -0^\circ.2 - 0^\circ.2$ .

- Using the existing catalog of the ATLASGAL dust continuum clumps at  $870 \mu\text{m}$  and the NVSS 1.4 GHz continuum map, a configuration of at least four H II regions (i.e. “system N36”; extension  $\sim 35 \text{ pc}$ ) is observationally found in the inner Galaxy at a distance of

6.0 kpc. These H II regions are G24.83+0.10 (containing two compact/ultra-compact H II regions G24.85+0.09 and G24.80+0.10), G24.74+0.08, G24.71-0.13, and G24.68-0.16.

- Each of the H II regions in the system is powered by a radio spectral type of O star. The dynamical ages of the H II regions vary between 0.4 and  $1.3 \text{ Myr}$  for  $10^3 \text{ cm}^{-3}$  ambient density.
- At least one 6.7 GHz methanol maser is detected toward three H II regions (i.e. G24.85+0.09, G24.80+0.10, and G24.68-0.16) in the system.
- The system N36 ( $l = 24^\circ.6 - 24^\circ.9$ ;  $d = 6.0 \text{ kpc}$ ) is located in the Milky Way where the Galactic bar meets the Norma Galactic arm (i.e., the bar-arm interface).
- In the *Herschel* temperature map, the extended temperature structure is observed toward the system of H II regions which is well traced in a temperature range of 23 to 30 K.
- Twenty seven ATLASGAL clumps are found in the system. Several clumps are identified with high bolometric luminosity ( $> 10^3 L_\odot$ ), and are massive ( $> 10^3 M_\odot$ ).
- Using the *Spitzer* color-color ( $[4.5]\text{--}[5.8]$  vs  $[3.6]\text{--}[4.5]$ ) space, 125 embedded protostars are identified in our selected target field, and majority of them are found toward the ATLASGAL dust clumps in the system.
- Using the GRS  $^{13}\text{CO}$  line data, the molecular gas associated with the system is studied in a velocity range of  $102\text{--}116 \text{ km s}^{-1}$ .
- The spatial distribution of the dust emission, molecular gas, and ionized emission suggests an impact of massive stars powering the H II regions in the system N36.
- The  $^{13}\text{CO}$  line data reveal two extended GMCs (i.e. C24.81+0.10 (around  $109 \text{ km s}^{-1}$ ) and U24.68–0.16b (around  $113 \text{ km s}^{-1}$ )) in the direction of the system N36. These two clouds are interconnected in the velocity space, and are separated by  $4\text{--}12 \text{ km s}^{-1}$  in velocity.
- A “Keyhole” feature in the cloud at  $103\text{--}110.5 \text{ km s}^{-1}$  (i.e. C24.81+0.10) and a “Key” feature in the cloud at  $111\text{--}115 \text{ km s}^{-1}$  (i.e. U24.68–0.16b) are identified in the system N36. A displacement of  $\sim 33.3 \text{ pc}$  enables a spatial fit between the Keyhole and Key features.
- Signposts of massive star formation (i.e. H II regions and 6.7 GHz methanol masers) are investigated at the common zones of the two clouds, where the embedded protostars are also traced.
- The observational results suggest the onset of the CCC process in the system N36. Adopting the collision at a viewing angle  $45^\circ$  to the line of sight, the lifetime of the collision is estimated to be  $\sim 2.7\text{--}8.2 \text{ Myr}$ .

Taking into account all the observational results, the existence of the H II regions in the system seems to be explained by the interaction of molecular clouds at the bar-arm interface. In the direction of the system N36, high-resolution and optically thin molecular line data will be useful to further gain more insights in the CCC process.

We thank the anonymous reviewer for a critical reading of the manuscript and several useful comments and suggestions, which greatly improved the scientific contents of the paper. The research work at Physical Research Lab-

oratory is funded by the Department of Space, Government of India. This publication made use of data products from the the Spitzer Space Telescope, which is operated by the Jet Propulsion Laboratory, California Institute of Technology under a contract with NASA. This publication makes use of molecular line data from the Boston University-FCRAO Galactic Ring Survey (GRS). The GRS is a joint project of Boston University and Five College Radio Astronomy Observatory, funded by the National Science Foundation (NSF) under grants AST-9800334, AST-0098562, and AST-0100793. The National Radio Astronomy Observatory is a facility of the National Science Foundation operated under cooperative agreement by Associated Universities, Inc. IZ is supported by the Russian Foundation for Basic Research (RFBR) grants No. 17-52-45020 and 18-02-00660.

## REFERENCES

- Anathpindika, S. V. 2010, *MNRAS*, 405, 1431  
 Anderson, L. D. & Bania, T. M. 2009, *ApJ*, 690, 706  
 Anderson, L. D., Bania, T. M., Jackson, J. M., et al. 2009, *ApJS*, 181, 255  
 Balfour, S. K., Whitworth, A. P., & Hubber, D. A. 2017, *MNRAS*, 465, 3483  
 Baug, T., Dewangan, L. K., Ojha, D. K., & Ninan, J. P. 2016, *ApJ*, 833, 85  
 Benjamin, R. A., Churchwell, E., Babler, B. L., et al. 2003, *PASP*, 115, 953  
 Benjamin, R. A., Churchwell, E., Babler, B. L., et al. 2005, *ApJ*, 630, 149  
 Beuther, H., Meidt, S., Schinnerer, E., Paladino, R., & Leroy, A. 2017, *A&A*, 597, 85  
 Bisbas, T. G., Tanaka, K. E. I., Tan, J. C., Wu, B., & Nakamura, F. 2017, *ApJ*, 850, 23  
 Bronfman, L. 2008, *Ap. Space Sci.*, 313, 81-85  
 Carey, S. J., Noriega-Crespo, A., Price, S. D., et al. 2005, *BAAS*, 37, 1252  
 Churchwell, E., Povich, M. S., Allen, D., et al. 2006, *ApJ*, 649, 759  
 Churchwell, E., Watson, D. F., Povich, M. S., et al. 2007, *ApJ*, 670, 428  
 Condon, J. J., Cotton, W. D., Greisen, E. W., et al. 1998, *AJ*, 115, 1693  
 Deharveng, L., Schuller, F., Anderson, L. D., et al. 2010, *A&A*, 523, 6  
 de Jager, C., Nieuwenhuijzen, H., & van der Hucht, K. A. 1988, *A&AS*, 72, 259  
 Dewangan, L. K., Ojha, D. K., Grave, J. M. C., & Mallick, K. K. 2015a, *MNRAS*, 446, 2640  
 Dewangan, L. K., Luna, A., Ojha, D. K., et al. 2015b, *ApJ*, 811, 79  
 Dewangan, L. K. 2017, *ApJ*, 837, 44  
 Dewangan, L. K., & Ojha, D. K. 2017, *ApJ*, 849, 65  
 Dewangan, L. K., Ojha, D. K., Zinchenko, I., Janardhan, P., & Luna, A. 2017a, *ApJ*, 834, 22  
 Dewangan, L. K., Ojha, D. K., & Zinchenko, I. 2017b, *ApJ*, 851, 140  
 Dewangan, L. K., Devaraj, R., & Ojha, D. K. 2018a, *ApJ*, 854, 106  
 Dewangan, L. K., Ojha, D. K., Zinchenko, I., & Baug, T. 2018b, *ApJ*, 861, 19  
 Elia, D., Molinari, S., Schisano, E., et al. 2017, *MNRAS*, 471, 100  
 Elmegreen, B. G., 1998, in *ASP Conf. Ser.* 148, *Origins*, ed. C. E. Woodward, J. M. Shull, & H. A. Thronson, Jr. (San Francisco, CA: ASP), 150  
 Evans, N. J., II, Dunham, M. M., Jørgensen, J. K., et al. 2009, *ApJS*, 181, 321  
 Flaherty, K. M., Pipher, J. L., Megeath, S. T., et al. 2007, *ApJ*, 663, 1069  
 Fujita, S., Torii, K., Kuno, N., et al. 2017, *arXiv:1711.01695*  
 Fukui, Y., Ohama, A., Hanaoka, N., et al. 2014, *ApJ*, 780, 36  
 Fukui, Y., Torii, K., Ohama, A., et al. 2016, *ApJ*, 820, 26  
 Fukui, Y., Torii, K., Hattori, Y., et al. 2018a, *ApJ*, 859, 166  
 Fukui, Y., Kohno, M., Yokoyama, K., et al. 2018b, *PASJ*, 70, 41  
 Furukawa, N., Dawson, J. R., Ohama, A., et al. 2009, *ApJL*, 696, L115  
 Getman, K. V., Feigelson, E. D., Garmire, G., Broos, P., & Wang, J. 2007, *ApJ*, 654, 316  
 Gutermuth, R. A., & Heyer, M. 2015, *AJ*, 149, 64  
 Habe, A., & Ohta, K. 1992, *PASJ*, 44, 203  
 Hartmann, L., Megeath, S. T., Allen, L., et al. 2005, *ApJ*, 629, 881  
 Haworth, T. J., Tasker, E. J., Fukui, Y., et al. 2015a, *MNRAS*, 450, 10  
 Haworth, T. J., Shima, K., Tasker, E. J., et al. 2015b, *MNRAS*, 454, 1634  
 Hou, L. G., Han, J. L., & Shi, W. B. 2009, *A&A* 499, 473  
 Hou, L. G. & Han, J. L. 2014, *A&A* 569, 125  
 Hu, B., Menten, K. M., Wu, Y., et al. 2016, *ApJ* 833, 18  
 Inoue, T., & Fukui, Y. 2013, *ApJL*, 774, 31  
 Jackson, J. M., Rathborne, J. M., Shah, R. Y., et al. 2006, *ApJS*, 163, 145  
 Jones, C. & Dickey, J. M. 2012, *ApJ*, 753, 62  
 Kantharia, N. G., Goss, W. M., Roshi, D. A., Mohan, N. R., & Viallefond, F. 2007, *J. Astrophys. Astr.*, 28, 41  
 Kendrew S., Simpson R., Bressert E., et al. 2012, *ApJ*, 755, 71  
 Kuchar, T. A. & Clark, F. O. 1997, *ApJ*, 488, 224  
 Lockman, F. J. 1989, *ApJS*, 71, 469  
 Mallick, K. K., Ojha, D. K., Tamura, M., et al. 2015, *MNRAS*, 447, 2307  
 McClure-Griffiths, N. M., & Dickey, J. 2007, *ApJ*, 671, 427  
 Molinari, S., Swinyard, B., Bally, J., et al., 2010, *A&A*, 518, L100  
 Molinari, S., Merello, M., Elia, D., Cesaroni, R., Testi, L., & Robitaille, T. 2016, *ApJ*, 826L, 8  
 Motte, F., Schilke, P., & Lis, D. C. 2003, *ApJ*, 582, 277  
 Nguyen Luong, Q., Motte, F., Schuller, F., et al. 2011, *A&A*, 529, A41  
 Ohama, A., Dawson, J. R., Furukawa, N., et al. 2010, *ApJ*, 709, 975  
 Ohama, A., Kohno, M., Hasegawa, K., et al. 2018a, *PASJ*, 70, S45  
 Ohama, A., Kono, M., Fujita, S., et al. 2018b, *PASJ*, 70, S47  
 Panagia, N., & Walmsey, C. M. 1978, *A&A*, 70, 711  
 Parker, Q. A., Phillipps, S., Pierce, M. J. et al. 2005, *MNRAS*, 362, 689  
 Prinja, R. K., Barlow, M. J., & Howarth, I. D. 1990, *ApJ*, 361, 607  
 Rathborne, J. M., Garay, G., Jackson, J. M., et al. 2011, *ApJ*, 741, 120  
 Reid, M. J., Menten, K. M., Zheng, X. W., et al. 2009, *ApJ*, 700, 137  
 Reid, M. J., Menten, K. M., Brunthaler, A., et al. 2014, *ApJ*, 783, 130  
 Robitaille T. P., Meade, M. R., Babler, B. L., et al. 2008, *AJ*, 136, 2413  
 Sano, H., Enokiya, R., Hayashi, K., et al. 2018, *PASJ*, 70, 43  
 Sato, M., Wu, Y. W., Immer, K., et al. 2014, *ApJ*, 793, 72  
 Schuller, F., Menten, K. M., Contreras, Y., et al. 2009, *A&A*, 504, 415  
 Simpson, R. J., Povich, M. S. Kendrew S., et al. 2012, *MNRAS*, 424, 2442  
 Stil, J. M., Taylor, A. R., Dickey, J. M., et al. 2006, *AJ*, 132, 1158  
 Szymczak, M., Wolak, P., Bartkiewicz, A., & Borkowski, K. M. 2012, *AN*, 333, 634  
 Tackenberg, J., Beuther, H., Henning, T., et al. 2012, *A&A*, 540, 113  
 Takahira, K., Tasker, E. J., & Habe, A. 2014, *ApJ*, 792, 63  
 Tan, J. C., Beltrán, M. T., Caselli, P., et al. 2014, in *Protostars and Planets VI*, ed. H. Beuther et al. (Tucson, AZ: Univ. Arizona Press), 149  
 Thompson M. A., Urquhart J. S., Moore T. J. T., Morgan L. K., 2012, *MNRAS*, 421, 408  
 Torii, K., Hattori, Y., Hasegawa, K., et al. 2017a, *ApJ*, 835, 142  
 Torii, K., Matsuo, M., Fujita, S., et al. 2017b, *PASJ*, 70, 51  
 Takahira, K., Shima, K., Habe, A., & Tasker, E. J. 2018, *PASJ*, 70, 58  
 Urquhart, J. S., Moore, T. J. T., Schuller, F., et al. 2013a, *MNRAS*, 431, 1752  
 Urquhart, J. S., Thompson, M. A., Moore, T. J. T. et al. 2013b, *MNRAS*, 435, 400



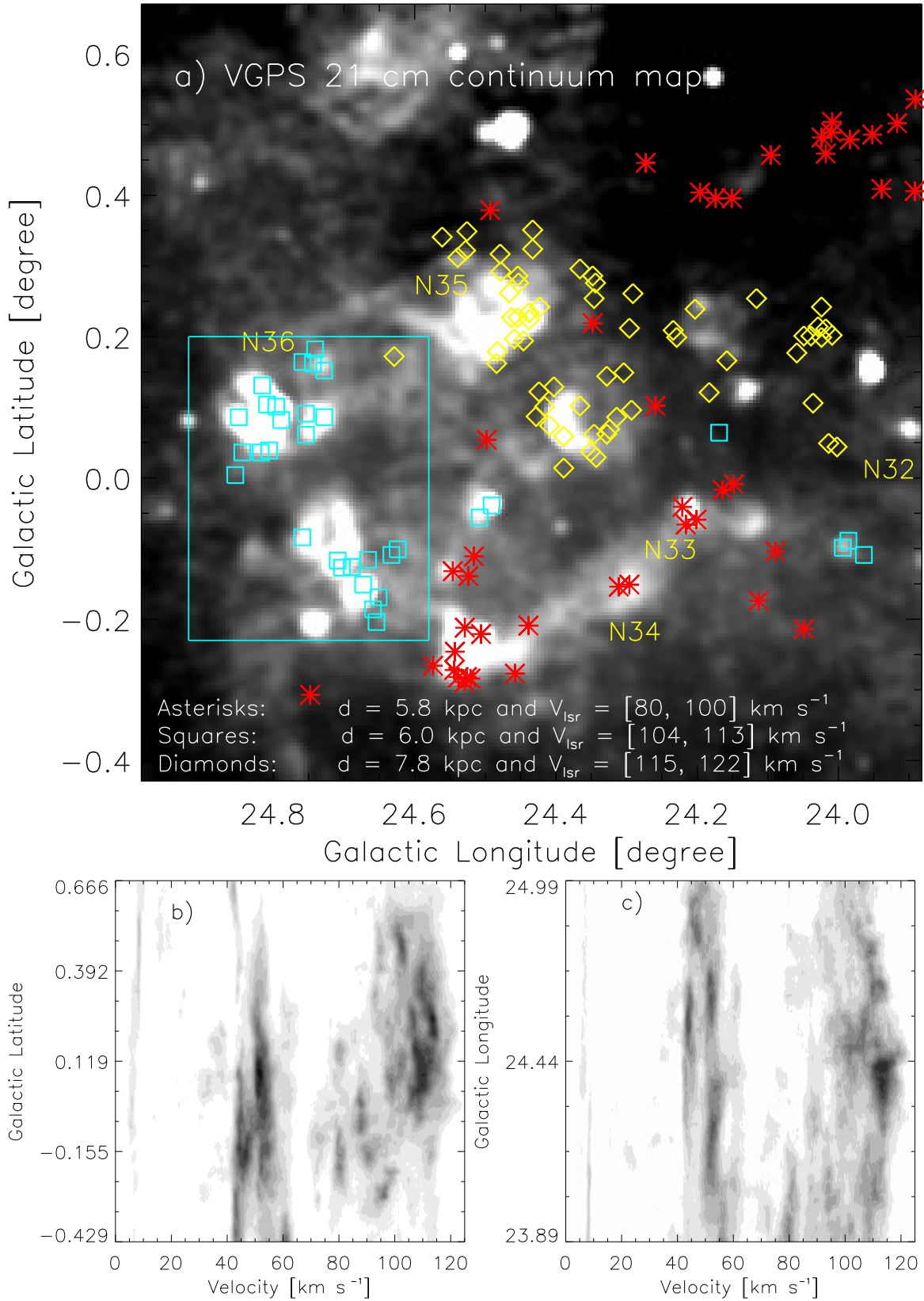


**Figure 1.** a) VGPS 21-cm continuum emission map (selected area  $\sim 1^\circ.1 \times 1^\circ.1$ ) toward  $l = 23^\circ.9 - 24^\circ.9$ . The ATLASGAL dust continuum clumps at  $870 \mu\text{m}$  (from Urquhart et al. 2018) are also overlaid on the map (see asterisk, square, and diamond symbols). The clumps highlighted with asterisks, squares, and diamonds are located at distances of 5.8, 6.0, and  $\sim 7.8$  kpc, respectively. Some previously known MIR bubbles (such as N32, N33, N34, N35, and N36; Churchwell et al. 2006) are also labeled in the map. The solid box (in cyan) refers to the area studied in this paper (see Figures 2a and 2b). b) Latitude-velocity map of  $^{13}\text{CO}$ . The  $^{13}\text{CO}$  emission is integrated over the longitude from  $23^\circ.89$  to  $24^\circ.99$  (see Figure 1a). c) Longitude-velocity map of  $^{13}\text{CO}$ . The  $^{13}\text{CO}$  emission is integrated over the latitude from  $-0^\circ.429$  to  $0^\circ.666$  (see Figure 1a). The position-velocity maps are shown in the velocity range from 0 to 125 km s $^{-1}$ . In all the panels, the longitude and latitude units are expressed in degrees.

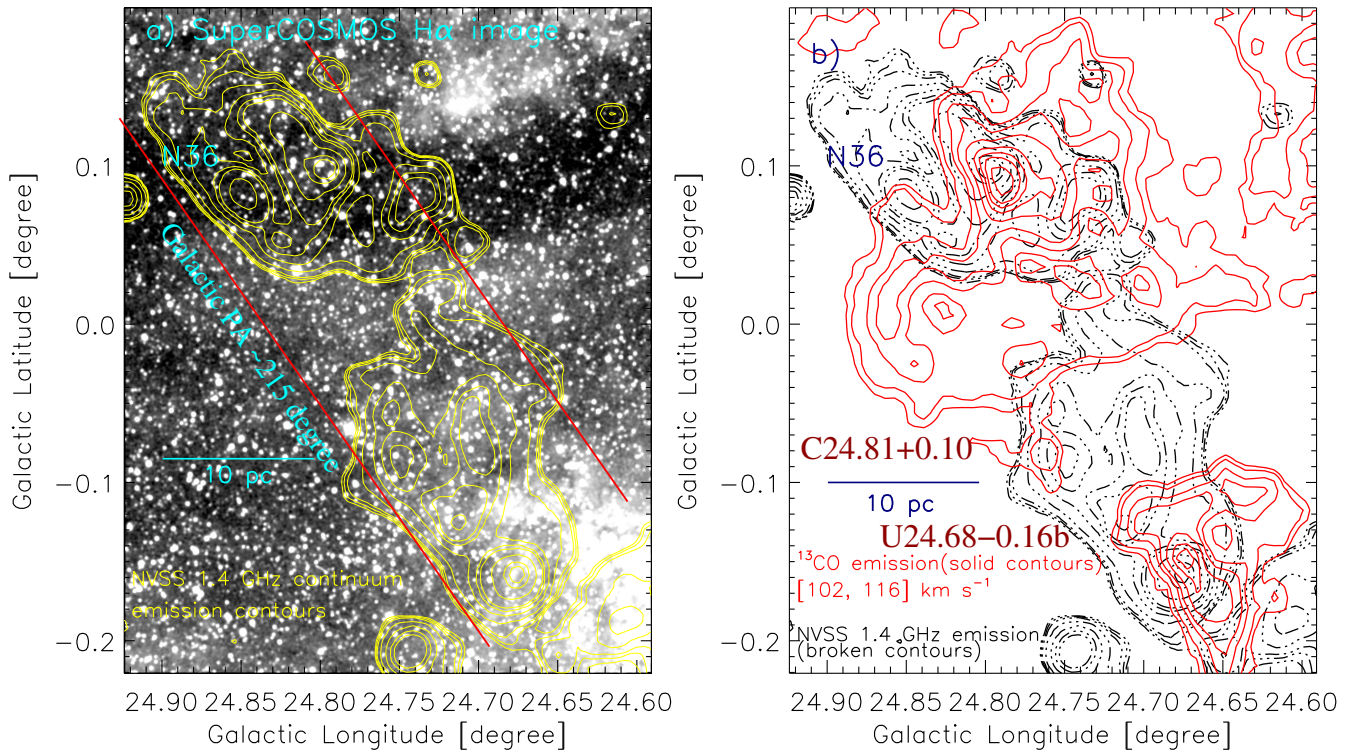


**Figure 2.** a) Overlay of the NVSS 1.4 GHz continuum emission contours ( $1\sigma \sim 0.45 \text{ mJy/beam}$ ) on the SHS H $\alpha$  image. The contours (in yellow) are shown with the levels of 2.5 ( $5.5\sigma$ ), 3.15, 4, 7.5, 18, 38, 60, 180, 450, and 650 mJy/beam. Each solid line (in red) is highlighted with a GPA of  $215^\circ$ . The SHS H $\alpha$  image is processed through a Gaussian smoothing function with a width of 4 pixels. b) Distribution of the  $^{13}\text{CO}(J=1-0)$  emission (in red) at  $[102, 116] \text{ km s}^{-1}$  against the NVSS 1.4 GHz continuum emission (in black). The  $^{13}\text{CO}$  emission contour levels (in red) are drawn with the levels of 12, 15, 22, 28, 38, 50, 58, 65, and 75  $\text{K km s}^{-1}$ . The NVSS broken contours (in black) are the same as in Figure 2a. The scale bar referring to 10 pc (at a distance of 6.0 kpc) is shown in the both the panels.

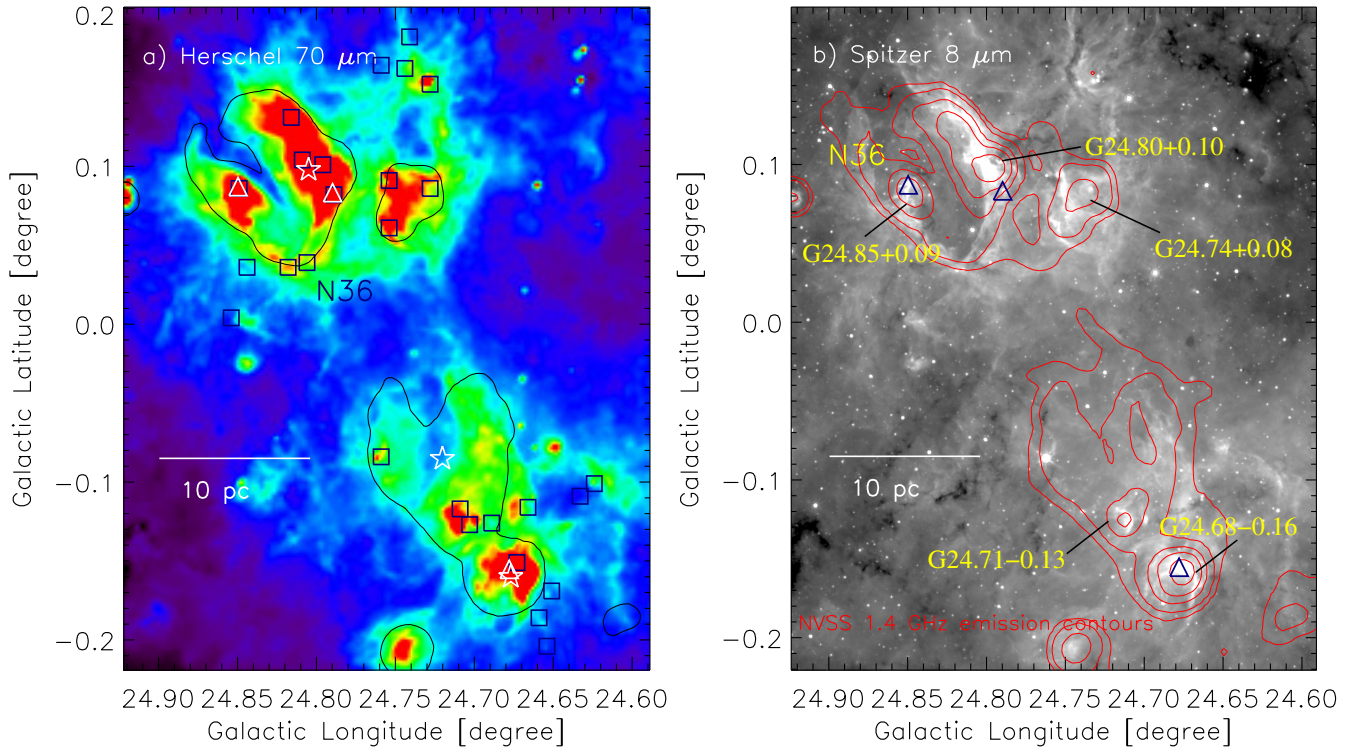


**Figure 3.** Distribution of warm dust, cold dust, and ionized emission toward the selected region in this paper (size  $\sim 0^{\circ}.33 \times 0^{\circ}.42$  ( $\sim 34.6$  pc  $\times$  44.0 pc at a distance of 6.0 kpc); central coordinates:  $l = 24^{\circ}.757$ ;  $b = -0^{\circ}.011$ ). a) Overlay of the ATLASGAL dust continuum clumps at 870  $\mu\text{m}$  on a false color *Herschel* 70  $\mu\text{m}$  image. The NVSS 1.4 GHz contour is also shown with a level of 16 mJy/beam. Twenty seven ATLASGAL clumps highlighted with squares ( $V_{lsr}$  range  $\sim 105$ – $114$  km  $\text{s}^{-1}$ ) are found at a distance of 6.0 kpc (see Table 2). Three stars (in white) indicate the positions of the RRL observations ( $V_{lsr}$  range  $\sim 108$ – $112$  km  $\text{s}^{-1}$ ; Lockman 1989). b) Overlay of the NVSS 1.4 GHz emission contours (in red) on the *Spitzer* 8.0  $\mu\text{m}$  image. The NVSS 1.4 GHz continuum contours are shown with the levels of 7.4, 18.6, 74.2, 185.6, and 464.1 mJy/beam. Several ionized regions (i.e G24.83+0.10 (hosting G24.85+0.09 and G24.80+0.10), G24.74+0.08, G24.71-0.13, and G24.68-0.16) are also marked in the figure. In both the panels, the positions of the Class II 6.7 GHz methanol masers (from Szymczak et al. 2012) are shown by triangles ( $V_{lsr}$  range  $\sim 110$ – $116$  km  $\text{s}^{-1}$ ).

Urquhart, J. S., König, C., Giannetti, A., et al. 2018, MNRAS, 437, 1059  
 Walsh, A. J., Burton, M. G., Hyland, A. R., & Robinson, G. 1998, MNRAS, 301, 640  
 Williams, J. P., de Geus, E. J., & Blitz, L. 1994, ApJ, 428, 693

Xu, Jin-Long, Li, Di, Zhang, Chuan-Peng, et al. 2016a, ApJ, 819, 117  
 Xu, Y., Reid, M., Dame, T., et al. 2016b, Science Advances, 2, e1600878  
 Yan, Q. Z., Xu, Y., Zhang, B., et al. 2016, AJ, 152, 117  
 Zinnecker, H., & Yorke, H. W. 2007, ARA&A, 45, 481

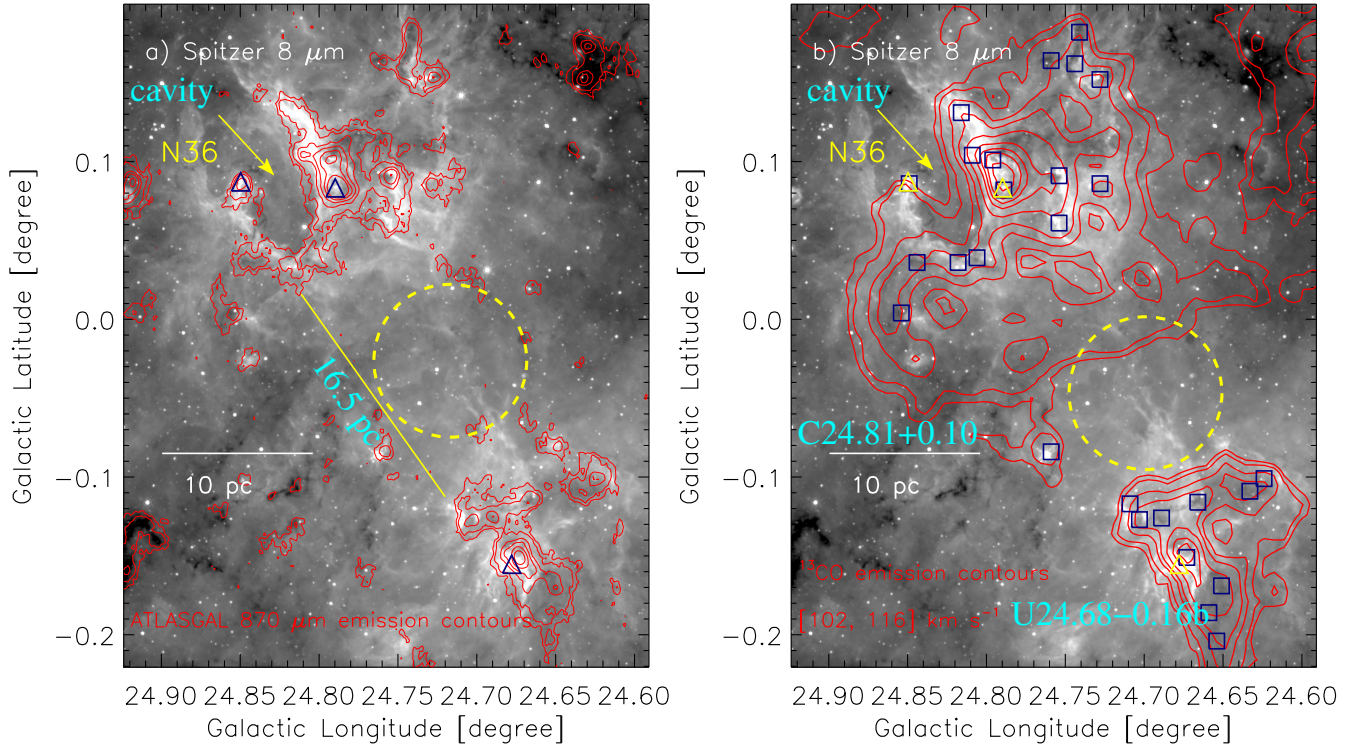


**Figure 4.** a) Overlay of the ATLASGAL 870  $\mu\text{m}$  continuum emission on the *Spitzer* 8.0  $\mu\text{m}$  image. The contour levels of the ATLASGAL 870  $\mu\text{m}$  emission are 15.2 Jy/beam  $\times$  (0.01, 0.02, 0.05, 0.08, 0.13, and 0.2). b) Overlay of the  $^{13}\text{CO}$  ( $J=1-0$ ) emission at [102, 116] km s $^{-1}$  and the ATLASGAL 870  $\mu\text{m}$  continuum clumps on the *Spitzer* 8.0  $\mu\text{m}$  image. The contour levels of the  $^{13}\text{CO}$  emission are 12, 15, 22, 28, 38, 50, 58, 65, and 75 K km s $^{-1}$  (see also Figure 2b). Other symbols are the same as in Figure 3. In each panel, a dashed big circle (in yellow) indicates an area without any molecular emission.

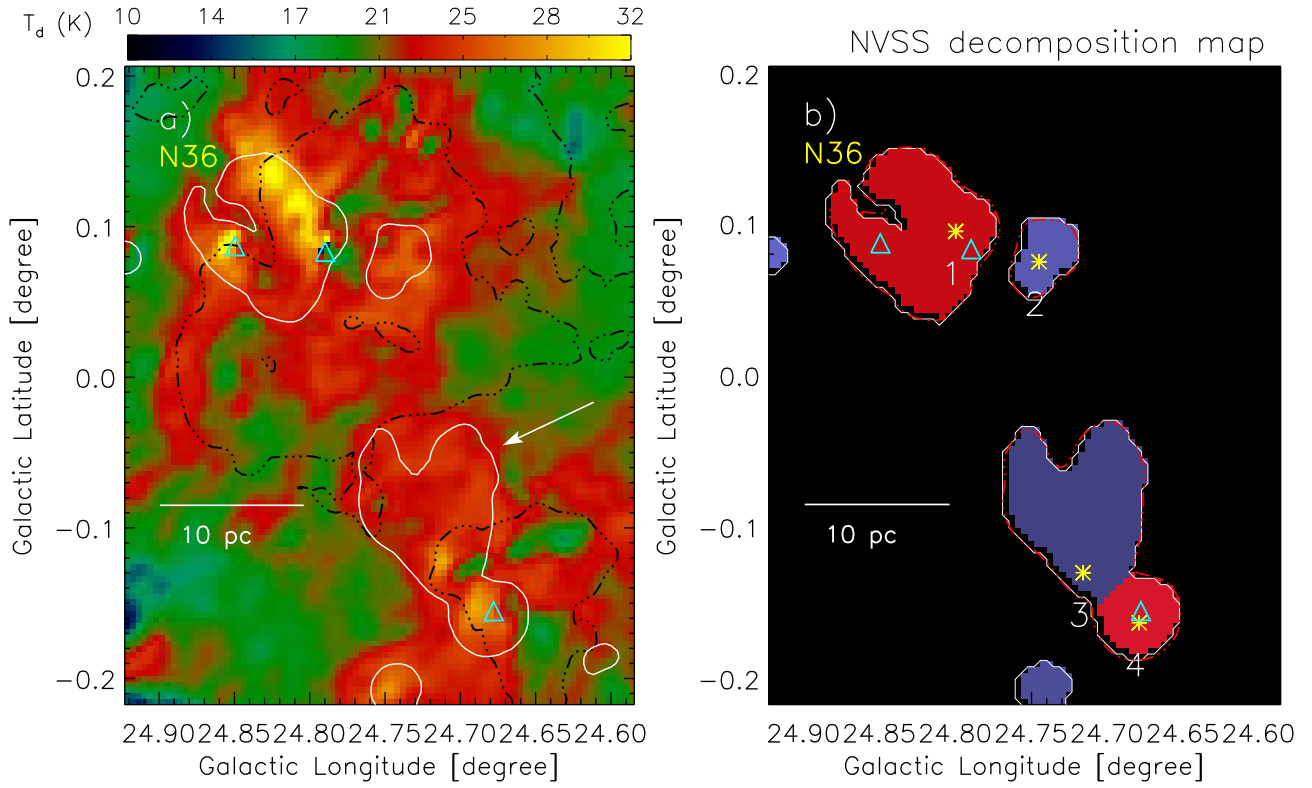


**Figure 5.** a) Overlay of the NVSS 1.4 GHz emission contour (in white) on the *Herschel* temperature map (resolution  $\sim 37''$ ). The  $^{13}\text{CO}$  ( $J = 1-0$ ) emission contour at  $[102, 116] \text{ km s}^{-1}$  (in black) is also shown with the level of  $12 \text{ K km s}^{-1}$ . An arrow indicates the presence of ionized emission between molecular clouds. b) Clumpfind decomposition of the NVSS continuum emission. The boundary of each identified H II region in the NVSS 1.4 GHz map is highlighted along with its corresponding ID and position (see asterisks and also Table 3). The NVSS 1.4 GHz emission contour with the level of  $0.016 \text{ Jy/beam}$  is also shown in each panel. In both the panels, the positions of the Class II 6.7 GHz methanol masers are shown by triangles (in cyan).

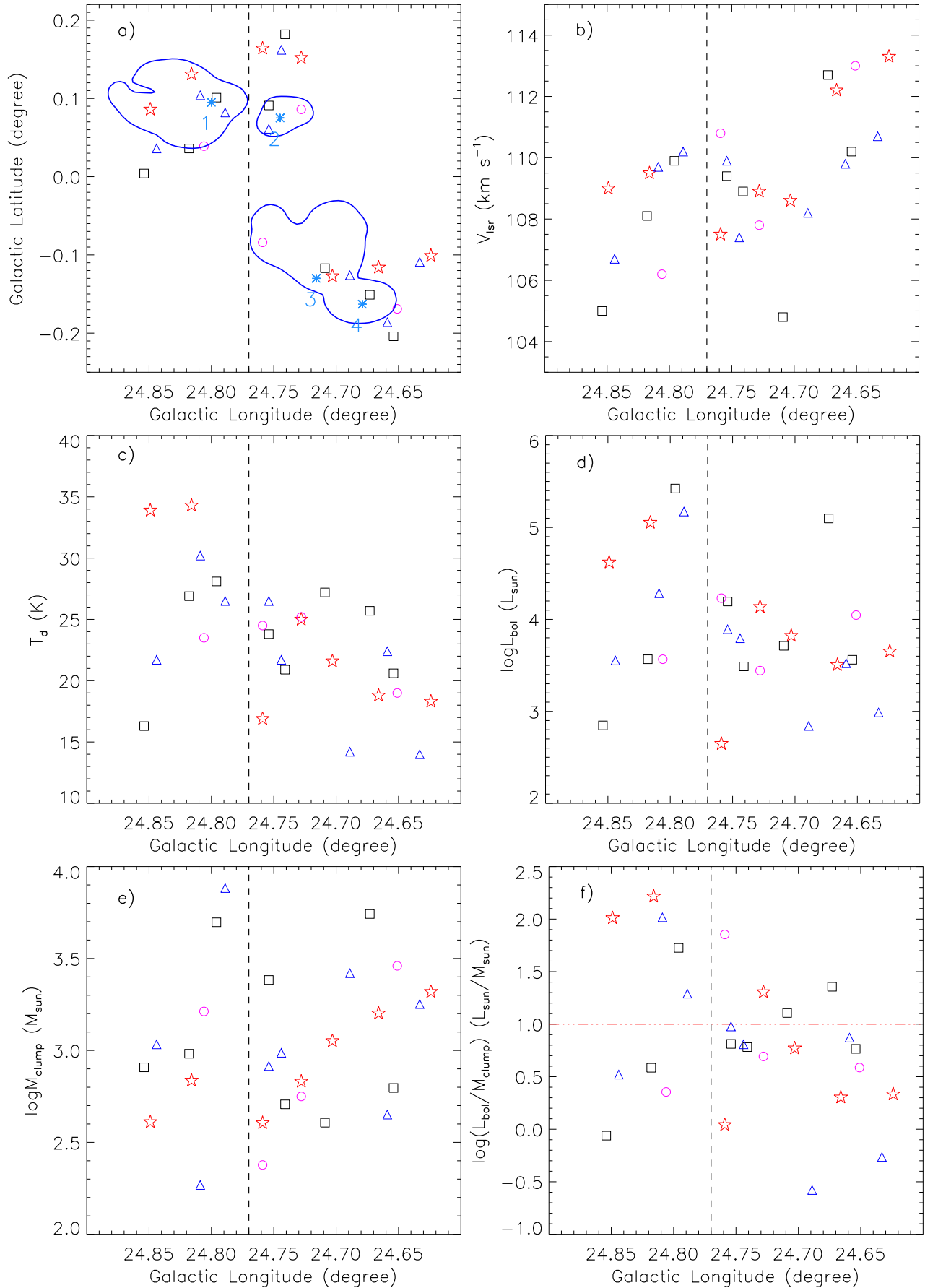


**Figure 6.** a) Distribution of 27 ATLASGAL dust continuum clumps at 870  $\mu\text{m}$  toward the selected region in this paper (see squares in Figure 3a). The positions of four H II regions are highlighted by asterisks and labeled in the figure (see Figure 5b). The NVSS emission toward these ionized regions is shown by blue curves. b-c-d-e-f) Distribution of the radial velocity, dust temperature, bolometric luminosity, mass, and ratio of the bolometric luminosity of clumps against the Galactic longitude. In each panel, four different symbols (i.e. squares, circles, stars, and triangles) indicate the dust clumps.

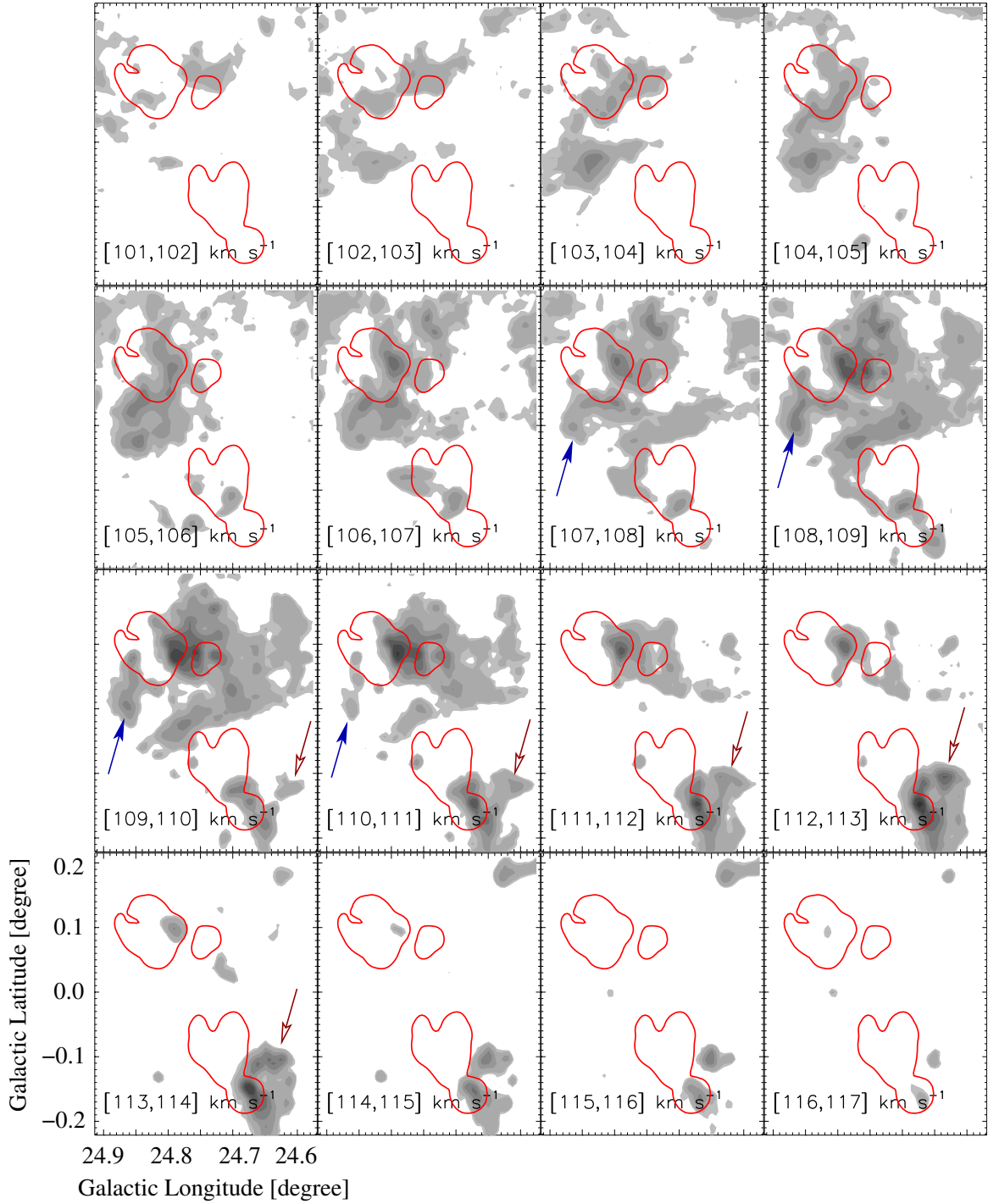


**Figure 7.** Velocity channel maps of the  $^{13}\text{CO}(J=1-0)$  emission. The molecular emission is integrated over a velocity interval, which is given in each panel (in  $\text{km s}^{-1}$ ). The contour levels are 1.5, 2, 4, 6, 8, 10, 12, and 15  $\text{K km s}^{-1}$ . In each panel, the red curves are the same as in Figure 6a. Molecular gas in two clouds is indicated by arrows.

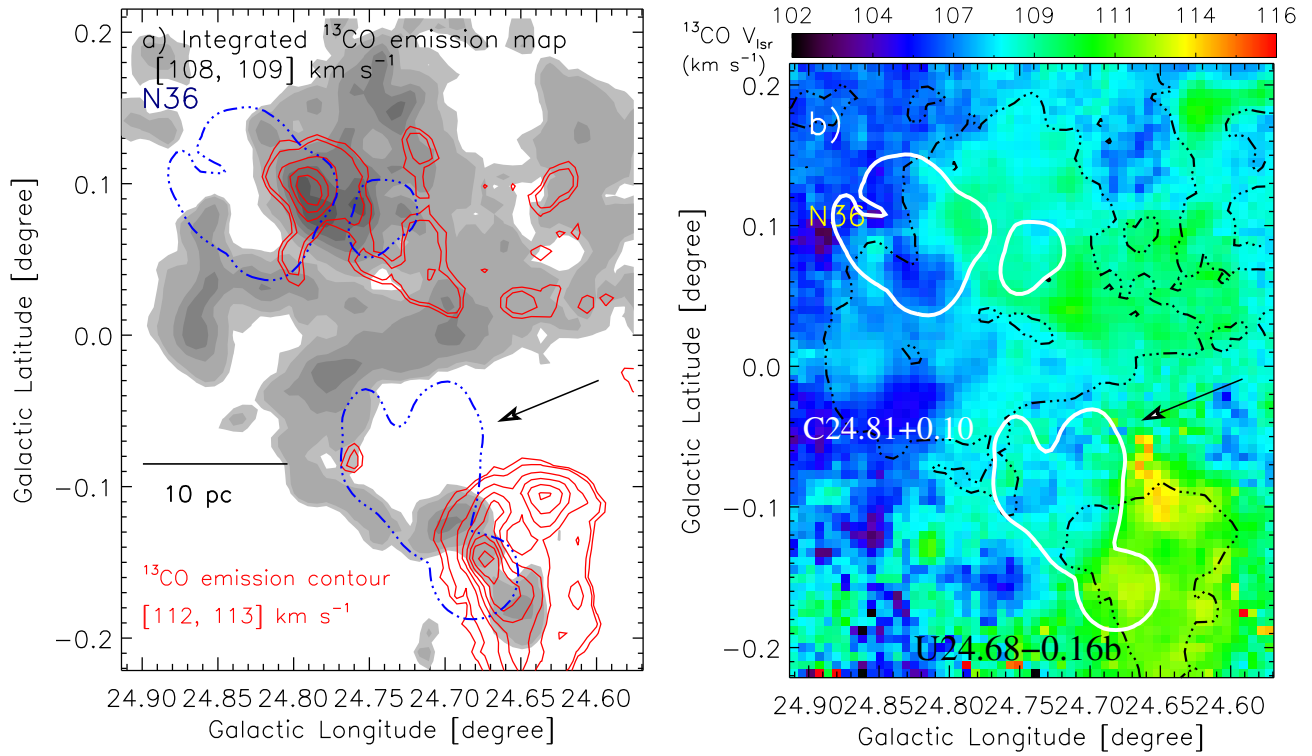


**Figure 8.** a) Spatial distribution of the  $^{13}\text{CO}$  emission integrated over two different velocity ranges (i.e. 108–109 and 112–113  $\text{km s}^{-1}$ ; see also Figure 7). The contour levels of the background molecular map (at 108–109  $\text{km s}^{-1}$ ) and molecular contours (in red; at 112–113  $\text{km s}^{-1}$ ) are the same as shown in Figure 7. b) Overlay of the  $^{13}\text{CO}$  emission at [102, 116]  $\text{km s}^{-1}$  on the GRS  $^{13}\text{CO}$  first-order moment map. The bar indicates the mean  $V_{\text{lsr}}$  in  $\text{km s}^{-1}$ . The  $^{13}\text{CO}$  emission contour is overlaid with a level of 12  $\text{K km s}^{-1}$ . In both the panels, the NVSS 1.4 GHz emission is highlighted by curves, which are the same as in Figure 6a. In each panel, an arrow indicates the presence of an extended ionized emission between molecular clouds.



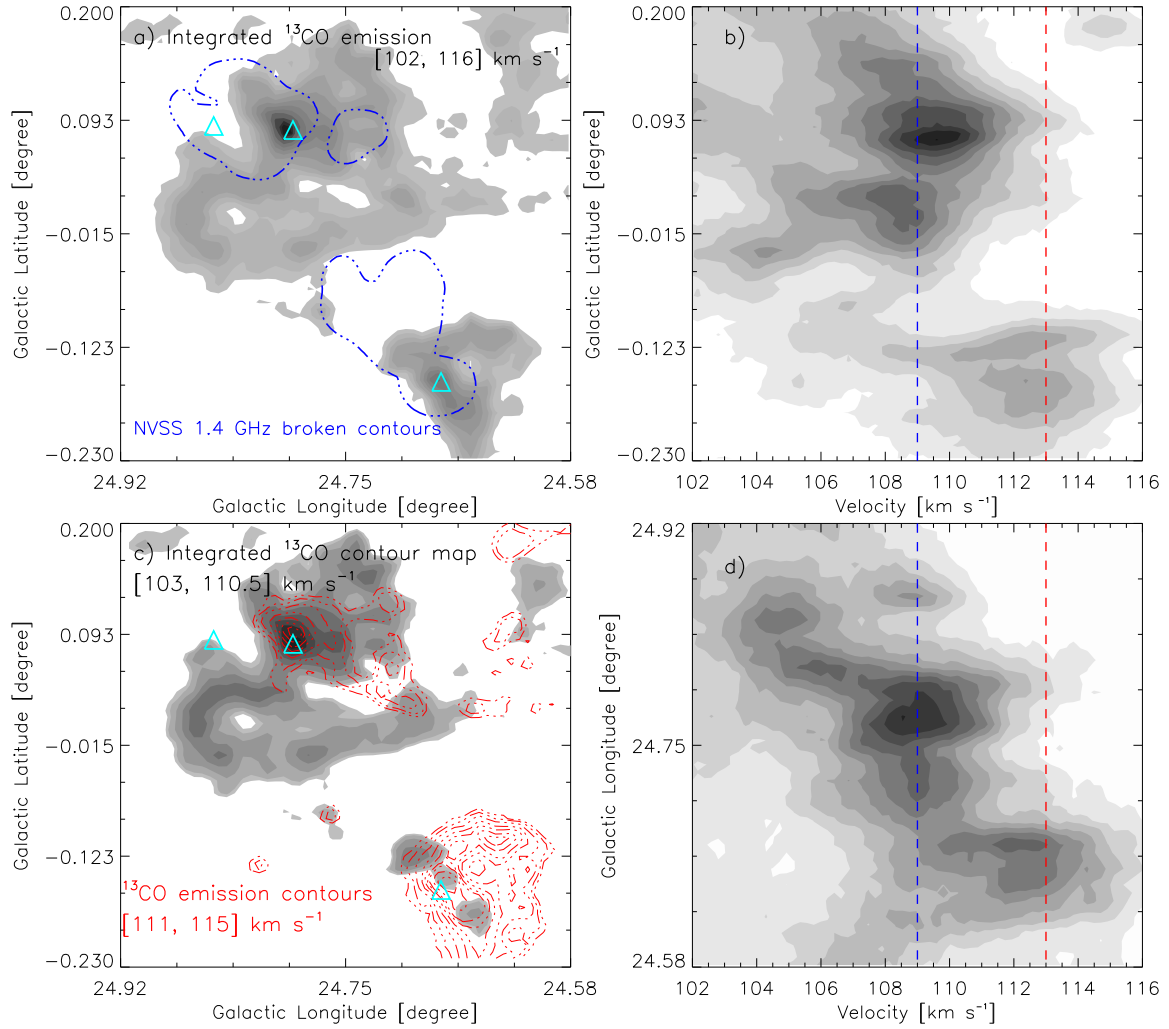


**Figure 9.** a) Integrated intensity map of  $^{13}\text{CO}$  ( $J = 1-0$ ) from 102 to 116  $\text{km s}^{-1}$ . The  $^{13}\text{CO}$  emission contour levels are the same as in Figure 4b. The broken blue curves are the same as in Figure 6a. b) Latitude-velocity map of  $^{13}\text{CO}$ . The  $^{13}\text{CO}$  emission is integrated over the longitude from  $24^{\circ}.58$  to  $24^{\circ}.92$ . c) The  $^{13}\text{CO}$  emission integrated over two different velocity ranges (i.e. 103–110.5 and 111–115  $\text{km s}^{-1}$ ) is presented, and the velocity ranges are also given in the figure. The contour levels of the background  $^{13}\text{CO}$  emission map are 10.5, 12, 15, 20, 25, 33, 40, 45, and 50  $\text{K km s}^{-1}$ , while the broken contours (in red) are 4, 5.5, 8, 12, 16, 20, 23, 30, and 38  $\text{K km s}^{-1}$ . d) Longitude-velocity map of  $^{13}\text{CO}$ . The  $^{13}\text{CO}$  emission is integrated over the latitude from  $-0^{\circ}.23$  to  $0^{\circ}.20$ . In both the left panels (i.e. Figures 9a and 9c), the positions of the 6.7 GHz masers are shown by triangles (in cyan). In both the right panels (i.e. Figures 9b and 9d), two velocities (i.e. 109 and 113  $\text{km s}^{-1}$ ) are highlighted by two dashed lines.

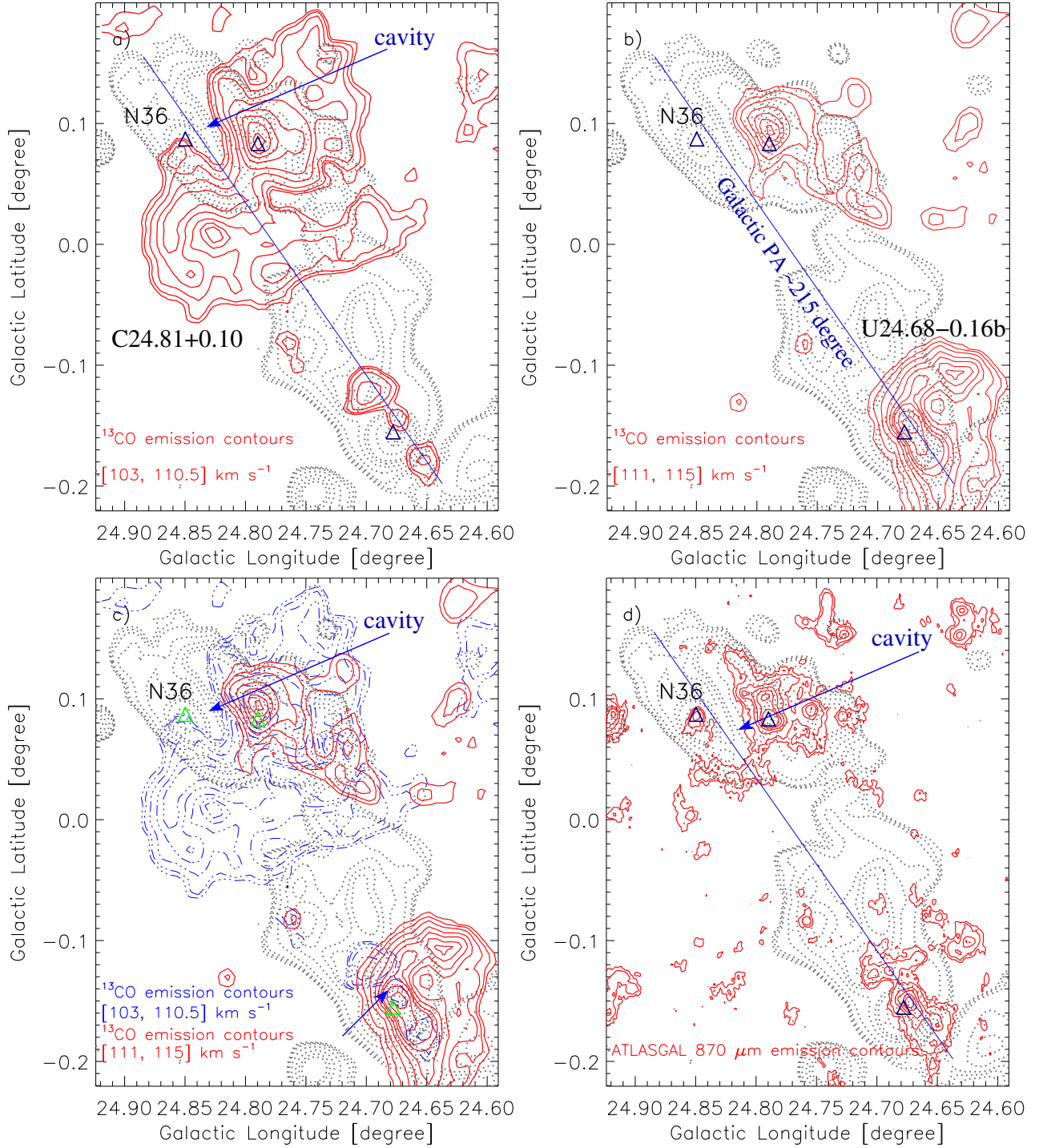


**Figure 10.** a) Spatial distribution of the  $^{13}\text{CO}$  emission at  $[103, 110.5] \text{ km s}^{-1}$  and the NVSS 1.4 GHz continuum emission (see Figures 2a and 9c). b) Spatial distribution of the  $^{13}\text{CO}$  emission at  $[111, 115] \text{ km s}^{-1}$  and the NVSS 1.4 GHz continuum emission (see Figures 2a and 9c). c) Spatial distribution of the  $^{13}\text{CO}$  emission integrated over two different velocity ranges (i.e.  $103\text{--}110.5$  and  $111\text{--}115 \text{ km s}^{-1}$ ) and the NVSS 1.4 GHz continuum emission (see Figures 2a and 9c). d) Spatial distribution of the continuum emission at ATLASGAL  $870 \mu\text{m}$  and NVSS 1.4 GHz (see Figures 2a and 4a). In three panels, a solid line is similar to as in Figure 2a. In all the panels, the positions of the 6.7 GHz masers are also shown by triangles.

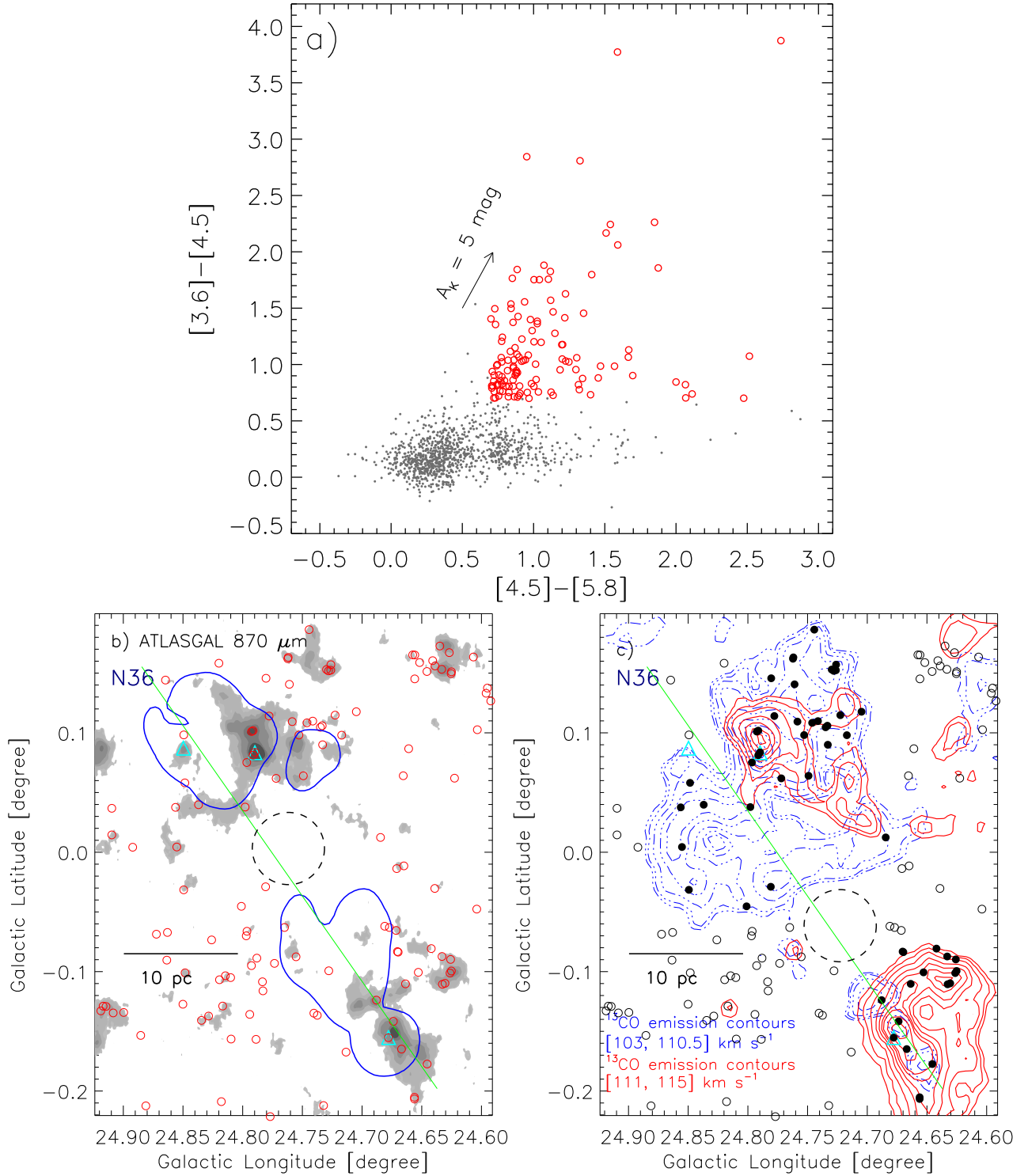


**Figure 11.** a) Color-color plot ( $[3.6]-[4.5]$  vs.  $[4.5]-[5.8]$ ) of sources observed in the our selected field. An extinction vector (from Flaherty et al. 2007) is shown in the figure. The dots (in gray) show the stars with only photospheric emission. Due to large numbers of stars with photospheric emission, we have plotted only some of these stars. The selected protostars are marked by red circles. b) Overlay of protostars (in red circles) on the ATLASGAL continuum map at  $870 \mu\text{m}$  (see also Figure 4a). The curves (in blue) are the same as in Figure 6a. c) Overlay of protostars (see circles) on the molecular intensity maps. The maps are the same as in Figure 10c. The protostars seen inside the clouds are shown by the filled circles (in black), while the protostars lying outside the clouds are represented by open circles (in black). In the panels “b” and “c”, the positions of the 6.7 GHz masers are also shown by triangles, and a dashed big circle indicates the gas-devoid area. In the panels “b” and “c”, a solid line is similar to as in Figure 2a.

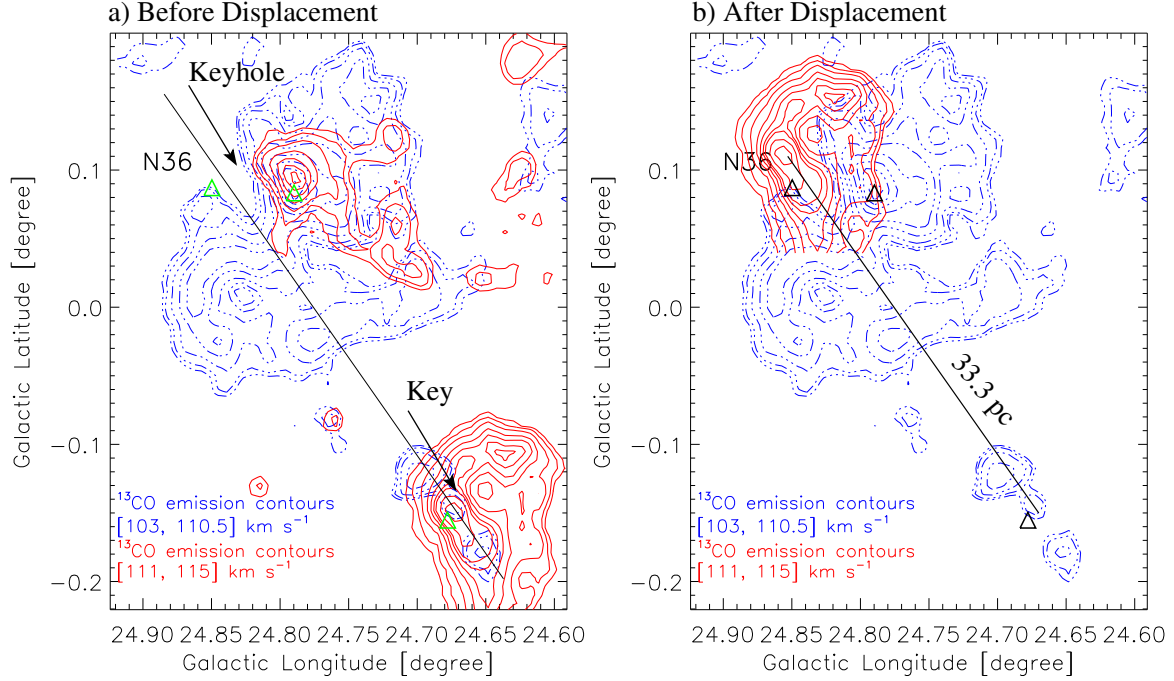


**Figure 12.** a) Spatial distribution of the molecular gas associated with clouds at [103, 110.5] and [111, 115] km s<sup>-1</sup>, similar to as in Figure 10c. b) Same as Figure 12a, but the cloud component at 111–115 km s<sup>-1</sup> is displaced in the northern direction along a line having the GPA of 215°.

**Table 2**

Physical parameters of the ATLASGAL dust clumps at 870  $\mu\text{m}$  (see Figure 3a). These parameters are taken from Urquhart et al. (2018). Table lists ID, Galactic coordinates ( $l$ ,  $b$ ), 870  $\mu\text{m}$  peak flux density ( $P_{870}$ ), 870  $\mu\text{m}$  integrated flux density ( $S_{870}$ ), radial velocity ( $V_{lsr}$ ), distance, clump effective radius ( $R_c$ ), dust temperature ( $T_d$ ), bolometric luminosity ( $L_{bol}$ ), clump mass ( $M_{clump}$ ), and H<sub>2</sub> column density ( $N(\text{H}_2)$ ).

ID	$l$ (degree)	$b$ (degree)	$P_{870}$ (Jy/beam)	$S_{870}$ (Jy)	$V_{lsr}$ (km s <sup>-1</sup> )	distance (kpc)	$R_c$ (pc)	$T_d$ (K)	$\log L_{bol}$ ( $L_{\odot}$ )	$\log M_{clump}$ ( $M_{\odot}$ )	$\log N(\text{H}_2)$ (cm <sup>-2</sup> )
c1	24.624	-0.101	1.34	9.07	113.3	6.0	2.93	18.3	3.653	3.319	22.584
c2	24.633	-0.109	0.86	5.06	110.7	6.0	1.61	14.0	2.988	3.252	22.578
c3	24.651	-0.169	1.33	13.28	113.0	6.0	3.21	19.0	4.047	3.460	22.556
c4	24.654	-0.204	0.45	3.24	110.2	6.0	0.70	20.6	3.561	2.796	22.033
c5	24.659	-0.186	0.58	2.62	109.8	6.0	0.70	22.4	3.523	2.651	22.091
c6	24.666	-0.116	0.86	7.22	112.2	6.0	1.68	18.8	3.506	3.202	22.373
c7	24.673	-0.151	4.83	39.11	112.7	6.0	4.82	25.7	5.098	3.742	22.929
c8	24.689	-0.126	1.32	7.63	108.2	6.0	1.61	14.2	2.841	3.420	22.753
c9	24.703	-0.127	1.14	6.26	108.6	6.0	1.88	21.6	3.823	3.052	22.407
c10	24.709	-0.117	0.51	3.09	104.8	6.0	0.70	27.2	3.713	2.607	21.920
c11	24.728	0.086	0.49	3.89	107.8	6.0	0.84	25.2	3.443	2.750	21.947
c12	24.728	0.152	1.32	4.63	108.9	6.0	2.16	25.0	4.137	2.831	22.382
c13	24.741	0.182	0.66	2.71	108.9	6.0	1.40	20.9	3.489	2.707	22.190
c14	24.744	0.162	0.78	5.44	107.4	6.0	2.30	21.7	3.795	2.987	22.240
c15	24.754	0.061	0.71	6.09	109.9	6.0	1.61	26.5	3.893	2.915	22.078
c16	24.754	0.091	2.09	15.45	109.4	6.0	2.37	23.8	4.195	3.383	22.611
c17	24.759	0.164	0.49	1.56	107.5	6.0	0.70	16.9	2.648	2.606	22.200
c18	24.759	-0.084	0.57	1.58	110.8	6.0	0.70	24.5	4.231	2.377	22.029
c19	24.789	0.082	15.52	56.56	110.2	6.0	2.93	26.5	5.173	3.883	23.418
c20	24.796	0.101	3.52	39.86	109.9	6.0	4.40	28.1	5.423	3.697	22.740
c21	24.806	0.039	0.64	10.23	106.2	6.0	2.58	23.5	3.567	3.212	22.105
c22	24.809	0.104	1.55	1.63	109.7	6.0	0.70	30.2	4.285	2.268	22.343
c23	24.816	0.131	0.75	7.11	109.5	6.0	3.35	34.3	5.053	2.837	21.957
c24	24.818	0.036	0.54	7.24	108.1	6.0	1.54	26.9	3.567	2.982	21.951
c25	24.844	0.036	0.58	6.06	106.7	6.0	1.68	21.7	3.553	3.033	22.111
c26	24.849	0.086	1.19	4.16	109.0	6.0	1.40	33.9	4.622	2.611	22.164
c27	24.854	0.004	0.57	2.95	105.0	6.0	1.68	16.3	2.847	2.908	22.290

**Table 3**

Physical parameters of four H II regions (see Figure 5b). Table lists ID, Galactic coordinates ( $l$ ,  $b$ ), deconvolved effective radius of the H II region ( $R_{\text{HII}}$ ), total flux ( $S_\nu$ ), Lyman continuum photons ( $\log N_{\text{uv}}$ ), dynamical age ( $t_{\text{dyn}}$ ), radio spectral type, electron density ( $n_e$ ), emission measure (EM), and mass of ionized hydrogen ( $M_{\text{HII}}$ ). Note that the extended H II region G24.83+0.10 hosts two compact/ultra-compact H II regions G24.85+0.09 and G24.80+0.10.

ID	$l$ (degree)	$b$ (degree)	$R_{\text{HII}}$ (pc)	$S_\nu$ (Jy)	$\log N_{\text{uv}}$ ( $\text{s}^{-1}$ )	$t_{\text{dyn}}$ (Myr)	Spectral Type (V)	$n_e$ ( $\text{cm}^{-3}$ )	EM ( $\text{cm}^{-6}$ pc)	$M_{\text{HII}}$ ( $M_\odot$ )	Other names
1	24.800	0.095	5.05	5.07	49.16	1.02	O6.5-O6	59	33160	785	G24.83+0.10
2	24.745	0.075	2.28	0.42	48.08	0.47	O9.5	56	13450	70	G24.74+0.08
3	24.716	-0.130	5.07	1.95	48.74	1.32	O7.5-O7	36	12620	490	G24.71-0.13
4	24.679	-0.163	2.66	1.89	48.73	0.41	O7.5-O7	94	44450	184	G24.68-0.16